

**Carrier Dynamics and Defects in GaAs and  
Related Photoconductors**

**Final Report**

Grant No. F49620-95-1-0227

March 1999

Prof. T.B. Norris  
Dr. J.F. Whitaker

University of Michigan  
Ultrafast Science Laboratory  
2200 Bonisteel Blvd., Room 1006  
Ann Arbor, MI 48109-2099

## REPORT DOCUMENTATION PAGE

0080

Public reporting burden for this collection of information is estimated to average 1 hour per response, including the gathering and maintaining the data needed, and completing and reviewing the collection of information. Send comment regarding this burden estimate or any other aspect of this collection of information, including suggestions for reducing this burden, to Washington Headquarters Services, Directorate for Information Operations and Reports, 1215 Jefferson Davis Highway, Suite 1204, Arlington, VA 22202-4302, and to the Office of Management and Budget, Paperwork Reduction Project (0704-0188), Washington, DC 20503.

1. AGENCY USE ONLY (Leave blank)		2. REPORT DATE 3/15/00		3. REPORT TYPE AND DATES COVERED Final Technical 3/15/95-8/31/98	
4. TITLE AND SUBTITLE Carrier Dynamics and Defects in GaAs and Related Photo Conductors				5. FUNDING NUMBERS  F49620-95-1-0227	
6. AUTHOR(S)  Theodore B. Norris and John F. Whitaker					
7. PERFORMING ORGANIZATION NAME(S) AND ADDRESS(ES) University of Michigan 3003 S. State St. Ann Arbor, MI 48109-1287				8. PERFORMING ORGANIZATION REPORT NUMBER	
9. SPONSORING / MONITORING AGENCY NAME(S) AND ADDRESS(ES) U.S. Army Research Office P.O. Box 12211 Research Triangle Park, NC 27709-2211				10. SPONSORING / MONITORING AGENCY REPORT NUMBER	
11. SUPPLEMENTARY NOTES The views, opinions and/or findings contained in this report are those of the author(s) and should not be construed as an official Department of the Army position, policy or decision, unless so designated by other documentation.					
12a. DISTRIBUTION / AVAILABILITY STATEMENT  Approved for public release; distribution unlimited.				12 b. DISTRIBUTION CODE	
13. ABSTRACT (Maximum 200 words)  Our program on Carrier Dynamics and Defects in GaAs and Related Photoconductors concentrated on two major thrusts: the study of the physical processes involved in trapping and recombination of carriers in low-temperature-MBE-grown (LT) GaAs, and the development of high-speed photoconductive probes. By using femtosecond time-resolved optical spectroscopy, with both above-gap and below-gap excitation and probing, we were for the first time able to measure the separate trapping times for electrons and holes, determine the lifetimes of the carriers within the traps, observe trap saturation, and observe an unusually large Auger recombination rate caused by the high density of crystal defects in LT-GaAs. The affects of surface passivation, materials growth conditions (temperature, annealing, and implantation) were studied. Two kinds of photoconductive devices were developed. A freely positionable voltage probe with picosecond time response, unprecedented sensitivity (30 nanovolts per root hertz), and high (micron) spatial resolution was developed. The same technology was adapted to develop a novel miniature source for terahertz radiation. The photoconductive probe was applied to the study of millimeter-wave devices and circuits.					
14. SUBJECT TERMS				15. NUMBER IF PAGES 48	
				16. PRICE CODE	
17. SECURITY CLASSIFICATION OR REPORT UNCLASSIFIED	18. SECURITY CLASSIFICATION OF THIS PAGE UNCLASSIFIED	19. SECURITY CLASSIFICATION OF ABSTRACT UNCLASSIFIED	20. LIMITATION OF ABSTRACT  UL		

## **I. Abstract**

Our program on Carrier Dynamics and Defects in GaAs and Related Photoconductors concentrated on two major thrusts: the study of the physical processes involved in trapping and recombination of carriers in low-temperature-MBE-grown (LT) GaAs, and the development of high-speed photoconductive probes. By using femtosecond time-resolved optical spectroscopy, with both above-gap and below-gap excitation and probing, we were for the first time able to measure the separate trapping times for electrons and holes, determine the lifetimes of the carriers within the traps, observe trap saturation, and observe an unusually large Auger recombination rate caused by the high density of crystal defects in LT-GaAs. The effects of surface passivation and materials growth conditions (temperature, annealing, and implantation) were studied. Two kinds of photoconductive devices were developed. A freely positionable voltage probe with picosecond time response, unprecedented sensitivity (15 nanovolts per root hertz), and high (micron) spatial resolution was developed. The same technology was adapted to develop a novel miniature source for terahertz radiation. The photoconductive probe was applied to the study of microwave and millimeter-wave devices and circuits.

## **II. Executive Summary**

In this final report we provide a summary of the work performed in the three-year program. We present the most important technical results of our research into the physics and applications of LT-GaAs and related materials. A substantial portion of these results have of course been presented in our three prior annual reports; we select here only what we consider to be the most important results and accomplishments, leaving details of the incremental advances to the annual reports.

Prior to the commencement of this program, LT-GaAs was already recognized for its potential impact in a number of areas of electronics and optoelectronics. Following the pioneering growth of GaAs by molecular beam epitaxy (MBE) at low temperatures (LT-GaAs) by Smith, Calawa and co-workers in 1988 [Smith 1988], nonstoichiometric GaAs and other III-V binaries and ternaries were found to exhibit a wealth of unique physical properties and device possibilities. The most interesting applications of this unique material have made use of its high resistivity and breakdown strength and/or its ultrafast (single- or sub-picosecond) carrier lifetimes. These properties are intimately linked with the presence of a high concentration of stoichiometry-related defects—arising in LT-GaAs from excess-As incorporation due to MBE growth at low substrate temperatures [Kaminska 1989].

A number of commercial devices have made use of this new technology. These include a

high-speed (7-ps) metal-semiconductor-metal (MSM) photodetector operating in the 400–900-nm-wavelength range (manufactured by Picometrix), and microwave transistors with LT-GaAs buffer layers (manufactured by Martin Marietta). Furthermore, the initial application of LT-GaAs in laboratory devices has enjoyed much success. For example, at the University of Michigan we have developed a new generation of ultrafast detectors and sampling gates, novel current probes, *in situ* optoelectronic signal generators, and picosecond high-voltage switches [Whitaker 1993]. In addition to these optoelectronic devices, other applications of nonstoichiometric semiconductors include electronic devices employing high-resistivity buffer layers [Smith 1988], and all-optical devices based on saturable absorption for laser mode-locking, range-finding, and optical switching [Benjamin 1994]. A number of principal factors determine optoelectronic device performance: transport issues such as carrier lifetime (including persistent “tails”), mobility (which affects responsivity), resistivity (which affects dark current), and contact interfaces. Other factors include crystal quality and wavelength-dependent absorption. The main concerns for electronic buffers are *essentially the same* as the transport and structural issues governing optoelectronic device performance, with an emphasis placed on the thickness dependence of electronic parameters, the limits to crystallinity, thermal stability (e.g., under implantation conditions), and localized defects. For all-optical devices, the main issues are the wavelength sensitivity, the required peak optical power, the strength of the saturable absorption, and the achievable contrast. ◀

Despite the successful development of useful electronic and optoelectronic devices based on LT-GaAs and related materials, prior to the commencement of our program there were a number of outstanding questions regarding the physics of photoconductivity and carrier trapping. In particular, the nature of the trapping and recombination mechanisms responsible for the fast carrier lifetime is central for the understanding and optimization of both ultrafast optoelectronic devices and electronic buffer layers. The dependence of the carrier dynamics on a wide range of parameters, including materials growth conditions, annealing, implantation, carrier density, etc., had yet to be investigated in a systematic way. Our program proposed to use ultrafast laser spectroscopy and picosecond photoconductivity to investigate these fundamental issues.

Additionally, our program also proposed to exploit the development of LT-GaAs for high speed photoconductive devices. Although a number of such applications had been previously demonstrated (including picosecond MSM detectors, high-voltage switches, and picosecond pulse voltage sources using lift-off technology), the achievement of practical LT-GaAs-based devices suitable for routine circuit and device measurements required further development.

As a result, our program had two main thrusts: (1) the investigation of the physics of carrier dynamics and defects in LT-GaAs and related materials, and (2) the exploitation of these unique properties for novel ultrafast photoconductive devices.

*Our most important accomplishments may be tabulated as follows:*

*1. Carrier Dynamics*

- (a) Most complete measurement of electron and hole trapping times in LT-GaAs and ion-implanted GaAs, and their correlation with material parameters (growth temperature, annealing conditions, ion implantation, and surface passivation) performed to date.
- (b) First observation of high-carrier-density effects in LT-GaAs including trap saturation and defect-assisted Auger recombination.
- (c) First measurements of carrier lifetimes within trap levels in LT-GaAs.
- (d) Demonstration of ultrafast optical probing of carrier dynamics near defects in GaAs in combination with high (200-nm) spatial resolution using a femtosecond near-field scanning optical microscope (NSOM).

*2. Applications of ultrafast photoconductivity*

- (a) Development of a novel freely positionable photoconductive voltage sampling probe, capable of measuring picosecond voltage waveforms with the unprecedented sensitivity of 15 nV/ $\sqrt{\text{Hz}}$  and with a spatial resolution of 1 micron. The probe is sensitive enough to measure voltage transients through passivation layers. The probe can also be used to launch ultrafast voltage pulses onto transmission lines or other devices.
- (b) Development of grafted LT-GaAs technology for ultrafast photoconductive sampling and pulse launching for microwave devices and circuits.
- (c) Development of a novel freely-positionable miniature source of free-space terahertz (THz) radiation.
- (d) Application of ultrafast photoconductive sampling to microwave device and circuit characterization.

The technical details regarding each of these accomplishments are presented below in section III.

### III. Technical Accomplishments

#### *III.A. Physics of Carriers in LT-GaAs*

Our research program builds on considerable work on the properties of nonstoichiometric layers—and especially attempts to understand their semi-insulating behavior and the short carrier lifetime. Two models currently exist to explain these properties: the deep-level point-defect model [Jager 1993] and the buried Schottky-barrier model [Warren 1991]. In the deep-level point defect model, the point defects, which are partly compensated by deep acceptors, control the electrical and ultrafast optical properties by keeping the Fermi level at mid-gap, as is found in bulk, semi-insulating GaAs. These defects serve as trapping sites to capture optically generated carriers. The point defects are present in increasing numbers as the growth temperature  $T_G$  is lowered [see, e.g. Look 1993a], and as excess arsenic is incorporated into the material. Of the point defects, only the As antisite  $\text{As}_{\text{Ga}}$  has been identified with certainty [Kaminska 1993], and even then it is not known whether the dominant defect is an isolated  $\text{As}_{\text{Ga}}$  or whether it is complexed with another defect [Look 1993b]. The deep donor and acceptor defects,  $N_D$  and  $N_A$ , determine the conductivity,  $\sigma$ , as well as both band conductivity,  $\sigma_b$  and hopping conductivity,  $\sigma_h$ .  $N_D$  and  $N_A$  are important when designing for low-dark-current detectors or for use as buffer layers in transistors.

When the arsenic-rich material is post-annealed at a temperature  $T_A$  much higher than  $T_G$ , the formation of larger defects, in particular As precipitates, occurs. The Schottky-barrier model argues that the semi-insulating behavior and short lifetime of LT-GaAs are the consequence of carrier depletion regions that surround the metallic As. The contention is that, for a density of precipitates large enough that the depleted areas overlap, the material becomes semi-insulating, while also attracting and trapping photoexcited carriers at the Schottky barriers.

Implantation of ions also results in the formation of deep-level defects which can serve as traps and recombination centers. The carrier lifetime can be controlled via the implant dosage and ion type. An additional factor affecting carrier dynamics is the presence of surface fields. The surface field can drive carriers into the bulk, away from the contacts, and both the responsivity and the speed of the device may suffer. It may also be the case that the surface field is responsible for the persistent tail often found in the response time of LT-GaAs.

In the following sections (III.A.1-4) we summarize the most important experimental results of our program which addressed these issues.

### *III.A.1 Interband Dynamics Probed by Femtosecond Spectroscopy*

In this section we describe the results of high-density pump-probe experiments to investigate the trapping versus recombination of carriers in LT-GaAs. This summary is based on work from the thesis of Tom Sosnowski, who was supported in part by the AFOSR program; the studies of annealed samples have been published in *Applied Physics Letters*.

#### *III.A.1.1 Experimental samples*

The LT-GaAs samples examined in this section were 1.5- $\mu\text{m}$ -thick layers grown by molecular beam epitaxy at Lincoln Laboratory at temperatures of 210, 220, 230, 250 and 270 degrees C. *In-situ* annealing was performed at 600 °C for 10 minutes on part of each wafer so that both annealed and as-grown samples were available. All materials were found to be crystalline by electron diffraction. The layers were lifted off their GaAs substrates by etching and mounted on fused silica substrates in order to perform differential transmission measurements.

#### *III.A.1.2 High-Carrier-Density Electron Dynamics in LT-GaAs*

This section describes measurements we made in an effort to better characterize the trapping dynamics in LT-GaAs. The differential transmission measurements employed high-fluence pump pulses that created electron densities in excess of the trap-state densities. For the annealed samples, a two-level rate equation including terms to model trap saturation dynamics accurately fitted the measured signals, allowing us to extract the free-electron and trapped-electron lifetimes. Also, at very high carrier densities we observed that for some samples the initial free-electron lifetimes actually decrease with increasing carrier density. This effect could be fit by including an Auger recombination term in the rate equations that is many orders of magnitude larger than the Auger coefficient for standard GaAs. Similar measurements on the as-grown samples and measurements attempting to characterize the hole-trapping dynamics could not be modeled with simple rate equations and these measurements are discussed later.

#### *III.A.1.3 Measurements*

The laser source for the measurements was a 250-kHz Ti:sapphire regenerative amplifier producing 4- $\mu\text{J}$ , 80-fs-duration pulses at 800 nm. The probe pulses were obtained by splitting off ten percent of the output beam, focusing it into a 3-mm sapphire crystal to generate a single-filament white-light continuum, and filtering the continuum with a 10-nm-bandwidth, 860-nm interference filter. The rest of the output beam was intensity-modulated at 2 KHz by a mechanical chopper and used as the pump pulse source. The pump and probe beams were attenuated and focused on the sample with spot sizes of 100 and 80  $\mu\text{m}$ , respectively. The transmitted probe beam was detected with a photodiode connected to a lock-in amplifier. Pump-pulse energies ranged from 0.4 to 80 nJ and the probe-pulse energy was typically 40 pJ.

For each sample we measured the differential transmission signal as a function of delay between pump and probe pulses for a range of pump fluences, typically from  $5 \times 10^{-6} \text{ J/cm}^2$  to

$1 \times 10^{-3} \text{ J/cm}^2$ . The dominant mechanisms through which the pump beam changes the transmission of the probe beam are band to band absorption bleaching and induced absorption from defect levels. Of these two signal components, the bleaching signal is predominant at high carrier densities, especially for the annealed materials. The 860-nm probe wavelength was chosen for two reasons: 1) The electron contribution to the absorption bleaching signal is a factor of twenty greater than the hole contribution, allowing us to isolate and examine the electronic response of the material. 2) Because we are probing states at the bottom of the conduction band, carrier cooling effects are evident in the rise time of the signal and not in its decay. This simplified the modeling and analysis of the signal decay by allowing us to ignore a potentially variable parameter.

#### III.A.1.4 Analysis

A set of normalized measurements for the 220 °C material, characteristic of those obtained for the annealed samples, is shown in Fig. 1. At low pump fluences the differential signal decayed exponentially, as expected, and the decay rate was independent of the pump fluence. As the pump fluence was increased, the relaxation slowed and became non-exponential as a result of the traps saturating or 'filling up'. For free-electron densities sufficiently larger than the trap density such that  $N_e \gamma_e \gg N_t \gamma_t$ , the decay actually became linear;  $dN_e/dt$  was independent of  $N_e$  and was determined solely by  $N_t \gamma_t$ . Here  $N_e$  represented the free-electron density,  $\gamma_e$  the unsaturated decay rate for an electron,  $N_t$  the trap density, and  $\gamma_t$  the rate an electron decays from the trapping state.

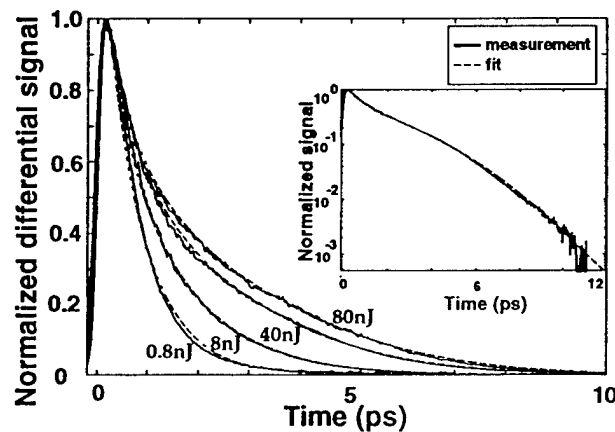


Figure 1. The differential signals (solid lines) and the fit curves (dashed lines) for the 220°C-grown GaAs sample with pump-pulse energies of 0.8 nJ, 8 nJ, 40 nJ and 80 nJ. (Fluences of  $10^{-5}$ ,  $10^{-4}$ ,  $5 \times 10^{-5}$  and  $10^{-3} \text{ J/cm}^2$ .) Inset: 40 nJ curve on a log scale.



A simple rate equation model, pictured schematically in Fig. 2, accurately reproduced the measured signal for the annealed samples. The normalized rate equations are as follows:

$$\frac{df_e}{dt} = \frac{g(t)}{N_0} - \gamma_e f_e (1 - f_t) - \alpha f_e^3 N_0^2 \quad (1)$$

$$\frac{df_t}{dt} = \eta \gamma_e f_e (1 - f_t) - \gamma_t f_t \quad (2)$$

In these equations  $g(t)$  is the electron generation term (representing the pump pulse),  $N_0$  is the initial carrier density,  $f_e$  is the fraction of injected electrons left in the conduction band,  $f_t$  is the fraction of traps which are occupied, and  $\eta$  is the ratio of  $N_0/N_t$ . The  $\alpha$  coefficient is related to the Auger process, which we ignore now but will discuss later.

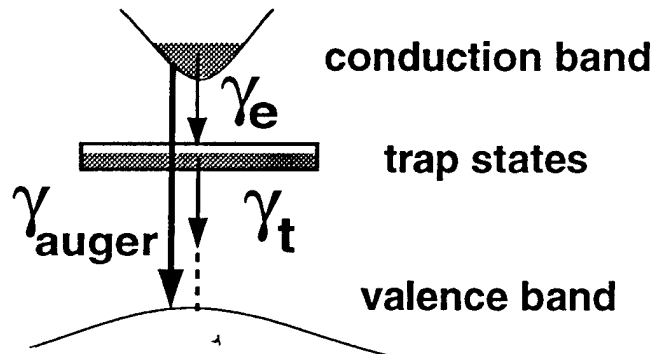


Figure 2. Schematic depicting the processes modeled by the rate equations, showing trapping of electrons and holes and recombination across the gap via Auger processes.

Three aspects of our modeling process should be mentioned. 1) Although the model fit the entire measured signal well, we were only interested in modeling the signal decay, so effects such as carrier cooling, which may be density dependent, did not have to be considered. 2) We could not predict from our measurements the fate of the trapped electrons – they may either recombine or decay to another trap state. 3) There was an induced absorption signal from defect levels present in the measurements evident as a negative signal with a decay time of several hundred picoseconds. The ratio of the magnitude of the negative signal to the peak positive signal was 7% for low fluence measurements on the 210 °C material. This ratio decreased for higher fluence measurements and for samples grown at higher temperatures. Because the negative signal was small and practically constant on the relevant time scales ( $1/\gamma_t \approx 10$  ps), we considered the negative signal level as the baseline to which the signal of interest decayed. (Note that the extremely different time scales of the trapped-electron lifetime and the decay of the negative signal indicated that the induced absorption signal could not be from the same defects that are predominantly responsible for the electron trapping.)

The model had three free parameters, neglecting the Auger term. For each sample, we determined  $\gamma_e$  by fitting the low-pump-fluence data with a single exponential. Then we selected  $\gamma_t$  so that the only parameter which needed to be varied to fit all the curves for a given sample was  $\eta$ . This simple model fit the experimental measurements very well for all pump fluence levels over almost three orders of magnitude as can be seen in Fig. 1, leading us to believe it accurately depicted the basic physical processes occurring in this material. Table 1 shows the fitting parameters for the annealed materials. Surprisingly, the trapped electron lifetimes decreased with increasing growth temperature (decreasing defect concentration). The uncertainty in the values arose from the fact that we were fitting a series of curves for each sample and the modeled signal was relatively insensitive to the  $\gamma_t$  parameter, especially when  $\gamma_t$  was significantly larger than  $\gamma_e$ .

material	270 °C	250 °C	230 °C	220 °C	210 °C
$\tau_e = 1/\gamma_e$	8 ps	2.3 ps	1.5 ps	0.75 ps	0.61 ps
$\tau_t = 1/\gamma_t$	0.5-3 ps	2-4 ps	1.5-2.5 ps	5-9 ps	15-25 ps

Table 1. Fitting parameters for free electron lifetimes and trapped electron lifetimes.

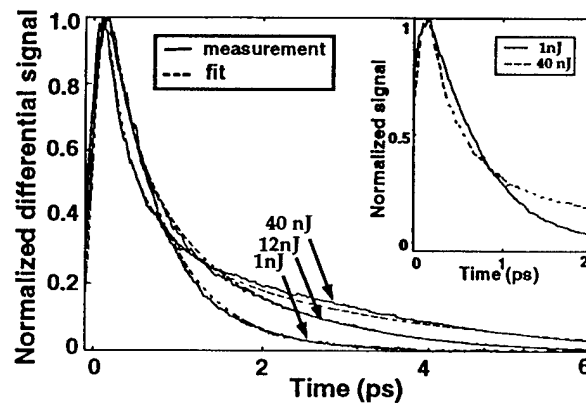


Figure 3. The differential signals (solid lines) and the fit curves (dashed lines) for the 210 °C-grown GaAs sample with pump-pulse energies of 1 nJ, 12 nJ and 40 nJ. The inset shows more clearly the increased initial decay rate in the high-fluence measurement.

For the 210 and 270 °C annealed materials the initial decay rate of the signal *increased* at very high carrier concentrations as shown in the inset of Fig. 3. Rate equations could not model this effect unless a carrier-density-dependent decay term was included. Two physical processes potentially able to explain the observed signals were Auger-assisted trapping and Auger-recombination. In Auger-assisted trapping the electron falls into the trap state and the excess energy is transferred to another free carrier. Since this process depends on only two carriers the rate at which this process occurs should be proportional to  $N^2$ , where  $N$  is the carrier density. Auger recombination involves three carriers and occurs when an electron and hole recombine non-radiatively and transfer their energy to another free carrier. The Auger recombination rate should be proportional to  $N^3$ . Incorporating Auger-assisted trapping into the model did not enable us to fit the data. The process turns on too slowly as a function of carrier density, and it could not produce a significant change in the initial decay rate because the electron traps rapidly fill and quench the process. Adding an Auger recombination term  $\alpha f_e^3 N_o^2$  enabled reasonable measurement fits as seen in Fig. 3. The Auger coefficients were estimated to be  $10^{-25}$  cm<sup>6</sup>/s and  $10^{-27}$  cm<sup>6</sup>/s for the 210 and 270 °C materials.

The measurements for the free-electron lifetimes agreed well with measurements made by us and other groups through both similar and different methods. The measurements for the trapped-electron lifetimes were rather surprising however, because they *decreased* for the materials grown at higher temperatures, and these samples should have a larger spacing between the defects. *This is opposite the dependence expected if the electrons and holes were recombining from spatially separated defects.* Two possible explanation were: the defects were more mobile and aggregate in the higher temperature materials so that on average electron and hole traps were actually closer together, or there were actually two defects primarily responsible for the trapping, *e.g.* O<sub>Ga</sub> and As<sub>Ga</sub><sup>+</sup>, that have similar cross sections but different trapped electron lifetimes, and their density ratio changed as a function of growth temperature. In terms of adding support to either the Schottky-barrier or point-defect models, *the fact that we can saturate the traps lends support to the point-defect model.* The anomalous trapped-electron lifetimes don't really lend support to either model at this time, but they are potentially explained through the behavior of point-defect-like traps. For both theories, the free-electron trapping rates were expected to be roughly proportional to the trap densities. This trend was supported by our data as shown in Table 2, displaying the free-electron lifetimes and the calculated electron trap densities (fit from the rate equations) for some of the samples. Comparison of the fitted electron densities with measured defect densities (by non-optical means such as EPR or zero quiescent bias voltage transient current spectroscopy) could allow the association of the electron trap states with specific defects, but measurements of these types have yet to be performed.

material	250 °C	230 °C	220 °C	210 °C
$\gamma_e$ (ps <sup>-1</sup> )	0.43	0.67	1.3	2.0
trap density (10 <sup>18</sup> cm <sup>-3</sup> )	0.26	0.5	0.8	1.2

Table 2. Comparison of the free-electron lifetimes and trap densities.

Recently, Siegner *et al.* [Siegner 1996] proposed that the dominant recombination pathway for trapped electrons is recombining with free holes. We believe this is not likely to be a dominant process. In their analysis, Siegner *et al.* assume the negative signal, with a time constant of 100's of picoseconds, is indicative of induced absorption from the primary trapping states; not necessarily a valid assumption in view of our results for the annealed materials. Also, if we model such a process and the rate-equation parameters are chosen to fit the signals for low and moderate pump fluences, the rate equations can not fit the much slower decay rates observed at high fluences. This is because at high carrier densities both the free-carrier decay rate and the trapped carrier decay rate are proportional to the number of free carriers so that the trapping bottleneck is not effective.

The Auger coefficients measured for the LT-GaAs samples were many orders of magnitude larger than the expected rate for GaAs. Auger recombination is normally restricted to materials with extremely high carrier densities and small bandgaps by momentum conservation requirements. A possible explanation for the increased Auger rates was that the large concentration of defects reduced the crystallinity of the material and relaxed the momentum conservation requirements for carrier scattering. The relaxation created a much wider range of energy states into which the excited electron may scatter, drastically increasing the Auger rate. The momentum relaxation  $\Delta k$  may be approximated by  $\Delta x^{-1} \propto n^{-1/3}$  where  $\Delta x$  is the average distance between defects and  $n$  is the defect density. For a defect density of 10<sup>18</sup> cm<sup>-3</sup>,  $\Delta k$  is 10<sup>6</sup> cm<sup>-1</sup>. (It is important to note that the electron and hole  $k$ -vectors are on the order of 5x10<sup>18</sup> cm<sup>-1</sup> at the wavelength where electron and hole contributions to the differential transmission signal are equal. Therefore, our claim that we can separately measure the electronic response of the material is still valid.)

#### III.A.1.5. Other Measurements

The 860-nm probe-beam signals from the as-grown samples were more complex and were not possible to fit with a two-level rate equation. Qualitatively, the signals were similar to those of the annealed samples as shown in Fig. 4; at low pump fluences the signal decayed

exponentially to a negative level, and at higher pump fluences the signal decay slowed down and developed a long positive tail. If a model similar to the one previously discussed could be loosely applied to as-grown LT-GaAs, it appears as if the trapped carrier lifetime also decreases with increasing growth temperature. However, even at very low pump fluences the signal could not be fit by a single time constant, and at higher pump fluences three or more time constants were observable. Also, the induced absorption contribution to the signal was much larger than in the case of the annealed samples; the magnitude of the negative and positive signal levels were in fact comparable. From this it was evident that the measured signal had large contributions from the variety of defect states present at high densities in the as-grown materials. Therefore, we could not expect to apply the simple rate equation model to these signals. Unfortunately, the details discernible from these types of differential transmission measurements were not sufficient to allow rate equation fits with a larger number of free parameters, and it was not clear what the physical significance of such models would be.

We have also attempted to characterize the hole trapping dynamics. Similar to being able to resolve the electron dynamics by probing near the band edge, using a probe wavelength of 745 nm should have made the measurements 10 times more sensitive to the hole densities than to the electron densities as shown by Tommasi *et al.* [Tomassi 1995]. Figure 5 shows differential transmission signals obtained for the 220 °C annealed material for a range of pump pulse fluences. Some differences with the 860-nm dynamics indicated that hole trapping likely contributed to the dynamics.

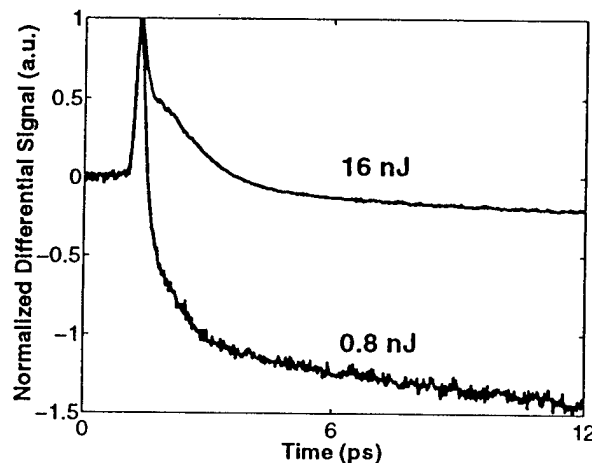


Figure 4. Differential transmission measurements (normalized to the peak positive signal) are shown for as-grown 220 °C samples for pump-pulse energies of 0.8 nJ and 16 nJ. Note the large negative tail, indicative of induced absorption, on the low-pump-energy measurement.

Unfortunately the simple rate equation model could not fit this data. Although the signals qualitatively show fast trapping and trap saturation, the fitting for the number of injected carriers remained approximately constant for fluences larger than  $200 \mu\text{J}/\text{cm}^2$ . Also, the differential signal with a 745-nm probe should have been around 60 times weaker than with an 860-nm probe for the same pump fluence levels, yet we observed only a factor of 10 difference. Because of this, we could not be completely sure at this time that our measurements were actually characterizing only hole dynamics, although the measurements did imply fast hole trapping. A possible explanation for the signal was that a large fraction of the 745-nm probe signal was due to reflectivity changes in the sample (because of changes in the index of refraction) as opposed to absorption changes. However this needs further investigation.

### III.A.1.6. Conclusion

In an effort to better understand the trapping dynamics in LT-GaAs we have performed differential transmission measurements on a series of LT-GaAs samples under conditions of high carrier densities. *For the annealed materials, fitting the electron measurement results with a two-level rate equation model allowed for the first time a measure of the trapped electron lifetimes as well as a measure of the free-electron lifetimes.* The measurements of the electron dynamics in the as-grown samples could not be fit with the two-level rate equation model and required more complicated analysis, reflecting the complex nature of the defects in unannealed LT-GaAs. The measurements with the 745-nm probe were

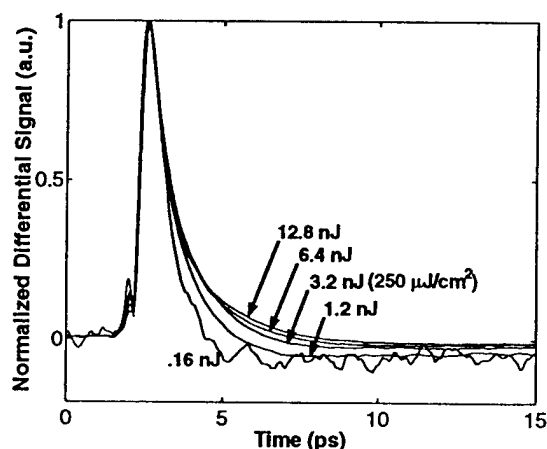


Figure 5. Differential transmission signals measured with an 800-nm pump and a 745-nm probe are shown for a range of pump-pulse energies. Notice for pump energies above 3.2 nJ the signal shape does not change much. (On a non-normalized scale the peak signal height increases linearly with the increasing pump energy for all of the signals shown here.)

inconclusive as well, and actually may not be measuring the quantitative hole dynamics as originally hoped (although they qualitatively imply fast, i.e. subpicosecond, hole trapping); further investigation will be required to understand these issues.

### III.A.2 Trap Dynamics Probed by Sub-gap Photoexcitation

Here we report results of femtosecond-resolution, time-resolved pump-probe experiments on annealed LT-GaAs samples grown at 210 and 300°C using sub-band-gap photon energy for the pump and/or probe beams. The goal of the experiment was to directly target the dynamics of sub-band-gap carriers, leading to new information on the carrier trapping and recombination times in the defect levels within the band gap. The sub-gap experiments were complementary to the saturation experiments described previously in this report, and in fact they appear to indicate the presence of traps that were not accessed when other wavelengths are used.

The samples investigated, as in Sect. A.1., were 1.5- $\mu\text{m}$ -thick MBE layers that were *in-situ* post-annealed at 600°C for 10 min. The films were removed from their native substrates by chemical etching and bonded to fused silica substrates to facilitate transmission measurements.

In the standard pump-probe measurements utilizing above-band-gap energy photons, a bleaching of the absorption was observed near the zero time delay due to free carriers photogenerated by the pump beam, i.e., the bandfilling effect. For LT-GaAs material, this bleaching typically recovered on a picosecond time scale, although the system virtually never returned to its ground state before several hundred picoseconds. It is very important to understand the nature of this long-lived excited state, since a slow carrier recombination time could severely limit the maximum repetition rate of optoelectronic devices made with this material.

First we will examine results of the sub-gap-photon-energy experiment for the LT-GaAs grown at 300°C, since the material has fewer defect states than material grown at lower temperatures and thus will yield insight into how the long-wavelength probe beam is sensitive to the different carrier excited states (Fig. 6). When  $\lambda_{\text{pump}} = \lambda_{\text{probe}} = 1.56 \mu\text{m}$  [Fig. 6(a)], a sharp rise in the absorption was observed at time zero (when pump and probe beams were coincident in time on the sample). This induced absorption was instantaneous, since it followed exactly the time profiles of the laser pulses. It was related to the two-photon absorption process, where one photon came from the pump pulse and the other from the probe pulse. This led to a depletion of the probe intensity, or an induced absorption, only when the pulses overlapped in time in the sample. The change in the index of refraction, on the other hand, was due to the interaction of the probe beam with the photogenerated free carriers. The decrease in the index in Fig. 6(a) was very small, and in particular about 200 times smaller than that in Fig. 6(b), where  $\lambda_{\text{pump}} =$

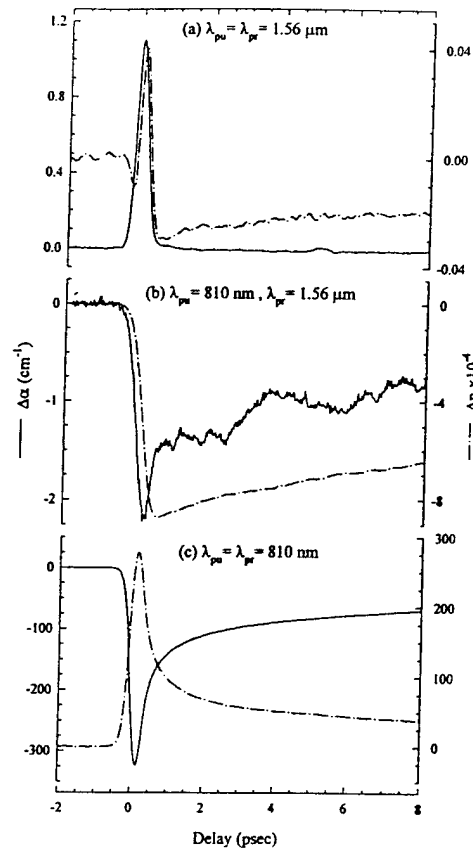


Figure 6. Transient absorption and index of refraction change for an LT-GaAs sample grown at 300°C and annealed at 600°C for 10 min. in situ. The three panels of the figure represent results using three different combinations of pump and probe wavelengths.

810 nm and  $\lambda_{\text{probe}} = 1.56 \mu\text{m}$ , and thus the linear and two-photon absorption at the long-wavelength could be considered to be very low in this sample. From Fig. 6(a), one could then tell from  $\Delta n$  that there were carriers photoexcited by two-photon absorption that were decaying from the conduction band, even though the absorption signal cannot distinguish this because it was sensitive to carrier absorption across the bandgap via two-photon absorption. There apparently were not trap states (or enough trap states) in this material that supported a transition excited by the 1.56- $\mu\text{m}$  probe light, or there would still be a response after the two-photon absorption signature in Fig. 6(a).

The situation for determining the carrier relaxation became somewhat clearer in Fig. 6(b) with  $\lambda_{\text{pump}} = 810 \text{ nm}$  and  $\lambda_{\text{probe}} = 1.56 \mu\text{m}$ , where the stronger signal was the  $\Delta n$ , which decayed with a relaxation time of 29 ps. Again, since the  $\Delta n$  signal was a signature of the carriers in the conduction band, this relaxation time was truly a measure of the free carrier relaxation time. This is likely, because of the short time scale involved, to also be the same as the carrier trapping time. When  $\lambda_{\text{pump}} = \lambda_{\text{probe}} = 810 \text{ nm}$  [Fig. 6(c)], both  $\Delta n$  and  $\Delta\alpha$  signals



were very large, because there was a strong absorption due both to band-to-band and free carrier absorption after the pump pulse arrived. Again, the long tail (on this 8-ps time scale) yielded a trapping time of 29 ps, while a reasonably sharp peak near time zero was also apparent. Since this peak was wider than that from two-photon absorption, and since our photon energy promoted electrons to an excited state approximately 100 meV above the conduction-band minimum, this peak could be attributed to carrier cooling. Since this peak was absent in Fig. 6(b) – at least for the case of  $\Delta n$  – we thus found that the long-wavelength probe beam was not sensitive to this excited state from which carriers rapidly cool.

For the annealed LT-GaAs grown at 210°C, the results were significantly different, primarily because of the dramatically increased density of mid-gap states resulting from the high concentration of defects in the material grown at the lowest temperatures before polycrystallinity was observed. Figure 7(a) shows a pulse with a peak that was substantially wider than that expected from a pump-probe cross-correlation [as in Fig. 6(a)]. This indicated that, for this sample, a significant number of carriers could be excited from the mid-gap defect states to the conduction band and/or from the valence band to the mid-gap states. Figure 7(b), when compared to Fig. 7(c), shows that a sub-bandgap probe-beam wavelength was more sensitive to the long-lived excited states that were related to defects.

In order to determine lifetimes of free and trapped carriers, a fitting routine based on a simple model including contributions from three individual carrier populations was developed. This allowed the decomposition of the experimental curves into contributions to the absorption from the populations of the different excited states [this is shown only in Fig. 7(b)].  $P_i(t)$  represented successive excited-state populations, decaying with the relaxation times  $\tau_i$ . A fit was not attempted with both the electron and hole densities, since that required a precise knowledge of the  $\Delta\alpha$  and  $\Delta n$  caused by each carrier type at each of their different excited states. Thus, each  $P_i(t)$  was composed of both electron and hole densities at a given stage of their relaxation, when they had similar relaxation times. Nevertheless, this phenomenological model allowed one to extract *every* component contributing to  $\Delta\alpha$  and  $\Delta n$  that had a different relaxation time.

Excellent fits, such as the one observed in Fig. 7(b), have been obtained from all of the experimental curves. They show, first of all, that there was an approximately 100-300 fs relaxation time  $\tau_1$  from  $P_1(t)$  for each combination of pump and probe wavelengths. This was carrier cooling, and it was also observed experimentally as the dominant feature of the  $\lambda_{\text{pump}} = \lambda_{\text{probe}} = 810$  nm condition of Fig. 7(c). The next relaxation time,  $\tau_2$ , associated with  $P_2(t)$ , was found to be between 0.7 and 1.2 ps, and it is believed that this corresponded to the carrier trapping time. The final populations,  $P_3(t)$  and  $P_4(t)$ , existed within mid-gap defects, and the associated time constants were related to trapped carrier lifetimes. The first trapped carrier lifetime,  $\tau_3$ , was approximately 10 ps in each case, and the final time constant ( $\tau_4$ ) was as long as

several hundred picoseconds. The latter time constant was routinely observed as the long negative tail in transient transmission experiments, and it indicated the presence of, at the least, a second trapping center that possessed a much longer relaxation (and apparently, recombination) time. This data demonstrated that there were at least two trap states that were responsible, in this type of LT-GaAs, for the relaxation from the conduction band to the valence band. This also confirms the results from the trap-saturation experiments, although the latter found slightly longer times for the relaxation time of the initial trap states in the same material.

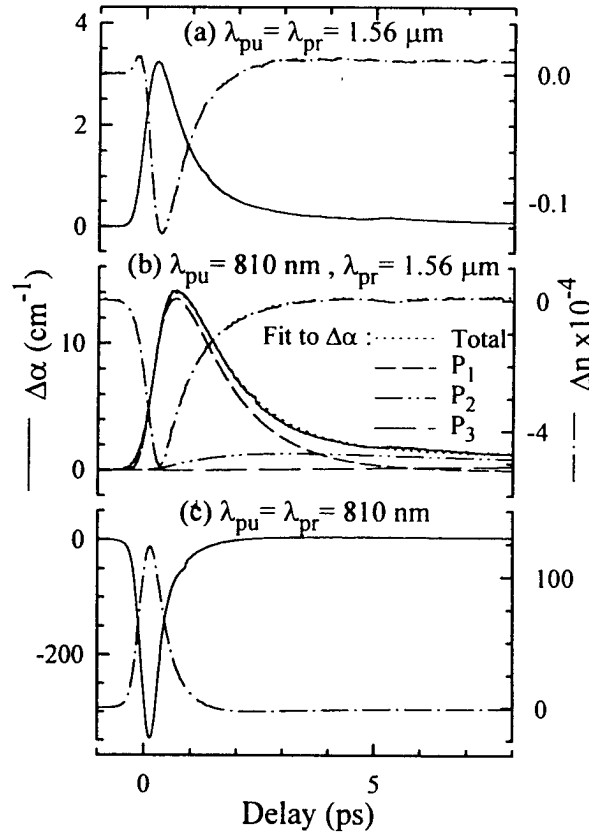


Figure 7. Transient absorption and index of refraction change for an LT-GaAs sample grown at 210°C and annealed at 600°C for 10 min. in situ. The three panels of the figure represent results using three different combinations of pump and probe wavelengths, and the curves labeled  $P_1$ ,  $P_2$ ,  $P_3$  and Total are calculated from a fitting procedure.

The trapping and recombination mechanisms and the nature of the defects responsible for these are still controversial. Arsenic-precipitate defects are believed by many to lead to recombination as soon as electrons and holes are trapped at the defect. Point defects, and especially As-antisites, are believed to yield a fast trapping time but also a slower recombination time. The latter hypothesis seems to apply to the behavior here. The  $P_3(t)$  population could result from electrons trapped at As antisites, while  $P_4(t)$  could be due to a shallow trap (e.g., an

As complex), and weak coupling of the defect to the GaAs matrix would explain the long  $\tau_4$  relaxation time. Whether such a long effective recombination time would severely limit the repetition rate of an optoelectronic device would depend on how many carriers each recombination channel (*i.e.*, each set of trapping states) can handle and on how much the saturation of one channel by carriers would affect the characteristics of the material. Our saturation experiments indicated that the first recombination channel could handle a high number of carriers, while the second saturated easily. Therefore, due to the low density of carriers trapped in the long-lived trapping states, only small perturbations to the material characteristic were expected on this  $> 100$  ps time scale. The possibility of a high density of trap states having lifetime  $\sim 10$  ps still raises uncertainty regarding ultra-high-repetition-rate-pulse or very-high-frequency detection.

### *III.A.3 Materials Issues – Ion-Implanted Semiconductors*

#### *(a) Arsenic-Implanted GaAs*

One approach to obtaining nonstoichiometric semiconductor material without resorting to low-temperature growth is to implant ions directly into the semiconductor. In a collaborative interaction with Lawrence Berkeley Lab, we showed how implantation of arsenic ions into GaAs could be used to create a material similar to LT-GaAs both in structure and in optoelectronic properties (see our first-year annual report). One major difference, however, was that the output of photoconductive switches fabricated on As-implanted GaAs had a voltage-dependent tail response that was not evident in LT-GaAs devices except at much higher bias fields. Since then we have found that the bias-dependent photoconductive transients could be represented by two relaxation time constants:  $T_1$  for the initial, fast exponential decay, and  $T_2$  for the second, longer exponential decay. We have also found conclusively for both As and Ar-implanted GaAs that the long  $T_2$  decay occurs as a result of carrier injection to the electrodes from the GaAs semi-insulating substrate.

As illustrated in Fig. 8, both  $T_1$  and  $T_2$  increased with the dc bias, but the  $T_2$ -dependence with bias was much stronger than that of  $T_1$ . This suggested that the two bias-dependent effects were due to different transport mechanisms. For the  $T_1$  relaxation, since it began immediately after the photoexcitation, the transient screening effect of photocarriers induced a field localization near the edges of the metal contacts. This led to a slight increase of the carrier capture time with increasing bias near the electrodes [Wang 1996]. A similar effect was also found in LT-GaAs photoswitches [Wang 1995]. In contrast, the second time constant,  $T_2$ , increased rapidly as the bias was raised from 5 V to 30 V, up to values of 10 ps at a bias of 20 V and 15 ps at a 30-V bias. While it was expected that there was rapid trapping in the region of the GaAs with precipitates and point defects, and probably also in an area with end-of-range defects,

it appeared that there was not a high enough defect density for the material implanted with one 200-keV dose (at  $10^{16} \text{ cm}^{-2}$ ) to trap all the photogenerated carriers before they reached the electrodes. Thus, the second time constant,  $T_2$ , became larger with increasing bias (and increasing attraction of the carriers to the contacts).

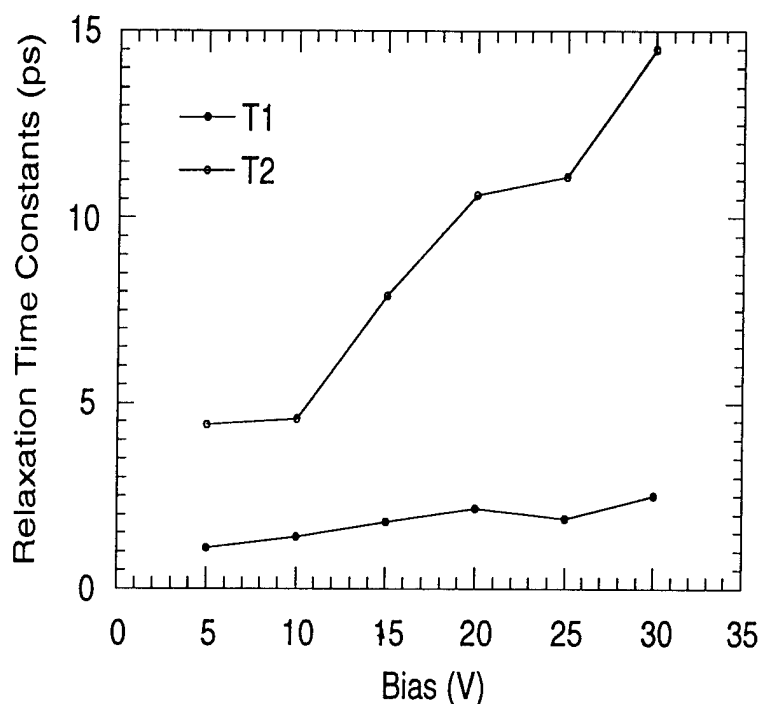


Figure 8. Two time constants of relaxation in an As-implanted GaAs photoconductive switch vs. bias.

To improve the performance of ion-implanted GaAs ultrafast photodetectors or pulse generators, and also to prove that the implanted layer was not responsible for the bias-dependent photoconductive tails, we felt it was necessary to remove the GaAs substrate from some of our singly-implanted devices. However, since there was no layer within the bulk implanted sample that could be used as a sacrificial etch-stop, a stoichiometric GaAs epitaxial layer was grown at 600 °C on top of an AlGaAs buffer. We then combined the As-implantation technology with epitaxial-lift-off (ELO) processing to isolate a thin-film, non-stoichiometric GaAs photoconductive device that was bonded onto an insulating fused-silica substrate. It was intended that this sample have the same excess As concentration as for the bulk devices, and the TEM characterization at LBL confirmed the presence of precipitates after annealing. The photoconductive response of a simple detector fabricated on the As-implanted ELO GaAs was measured via external electro-optic sampling and is shown in Fig. 9. The pulses had  $1/e$  fall times of approximately 460 fs and total FWHM durations of 700 fs. It was clearly observed that

the long, bias-dependent components from the bulk devices were now negligible. This was true over all bias values up to 30 V, although waveforms only up to 20 V are shown. *Therefore, this experiment conclusively showed that the major contribution of the second, persistent photocurrents observed in the two As-implanted bulk GaAs detectors were indeed due to photoexcited carriers injected from the substrate.* In addition, the As-implanted layer isolated from its substrate appeared to have very similar temporal response properties to LT-GaAs grown in the 210 °C range. *However, it was still true that the resistivity of the lift-off As-implanted GaAs layer was more than 10 times less than that of LT-GaAs, and the dark current was also roughly 7 times higher than that of typical LT-GaAs.*

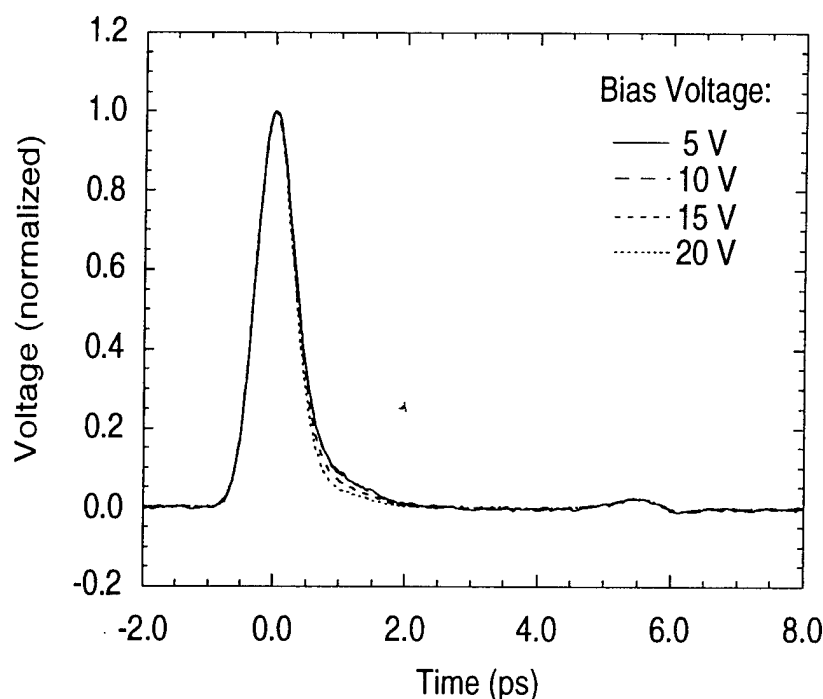


Figure 9. Photoconductive response of a thin-film, As-implanted GaAs switch fabricated on a fused silica substrate using the epitaxial-lift-off process.

## (b) Argon-implanted GaAs

In addition, in a further interaction with LBL and UC-Berkeley, we jointly investigated the optoelectronic and structural properties of GaAs layers that were implanted with Ar ions (200 keV and  $10^{16}$  cm $^{-2}$ ). *In a striking discovery, we determined that a subpicosecond decay of photoconductivity, a high resistivity, and a moderate mobility could all be attained in an ion-implanted, annealed GaAs layer that had no arsenic precipitates, but rather voids.* These voids, which have diameters between 3 and 5 nm, were not expected to accumulate a large excess charge or to form depletion regions. However, Berkeley measured via magnetic circular dichroism (MCD) that at the annealing temperature used (600 °C), there was still a large concentration of charged arsenic antisites. At the least, this demonstrated that a material exhibiting similar properties to those of arsenic-rich GaAs could be synthesized without adding extra arsenic via LT-MBE or implantation, and thus also without arsenic precipitates. However, it also provided evidence suggesting that point defects could play a prominent role in ultrafast trapping and high resistivity even after annealing, since there were no precipitates to aid recombination and presumably no depletion regions to decrease conduction.

The ultrafast photoconductive response, shown in Fig. 10 for several bias values, was once again measured on a device that utilized an ELO layer that had been implanted with ions in order to avoid deleterious substrate effects. The negative tail and small features trailing the pulse were due to the presence of the electro-optic probe and/or other time domain reflections from the surrounding transmission line structure.

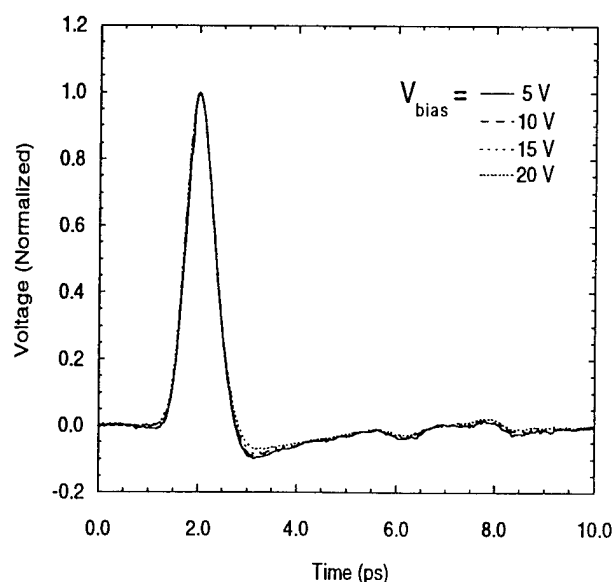


Figure 10. Photoconductive response of a thin-film, Ar-implanted GaAs switch fabricated on a fused silica substrate using the epitaxial-lift-off process.

(c) Gallium-implanted GaAs

Also in association with LBL and UCB, Ga was implanted in GaAs in order to investigate excess Ga in the form of anti-sites, interstitials, or semi-metallic Ga precipitates. GaAs was implanted with the same 200 keV energy at  $10^{16} \text{ cm}^{-2}$  as for the As and Ar implantation. At a 5 V bias, the dark current in a simple detector was four orders of magnitude higher for the device on the Ga-implanted GaAs than for one on As-implanted GaAs. It was not determined which Ga-related defect was responsible for this behavior. However, two possibilities were that hopping conduction took place between Ga interstitials or that excess Ga atoms in GaAs (as in Si or Ge) acted as relatively shallow acceptors so that the whole implanted region became p-type. Since the Ga-implanted GaAs was so conductive, it also seems possible that the comparatively low resistivity of As-implanted GaAs compared to LT-GaAs could have been due to the existence of Ga defects.

The entire ion-implanted-GaAs program is significant both in terms of the evidence it has supplied for the physical interpretation of the behavior of high-defect-density materials and especially for the production of new ultrafast optoelectronic devices. For use in picosecond or subpicosecond switches, detectors, and sampling gates, As or Ar-implanted GaAs may, in certain circumstances, be a reasonable alternative to LT-GaAs. Its greatest appeal may be its flexibility, from the standpoint that ion implantation of selected regions of a circuit, in order to locate an ultrafast device or to change the resistivity of an element, would be possible. On a semi-insulating substrate, for instance, one might wish to produce one device with a step-function response, and another with a subpicosecond response. This could be easily accomplished by implanting As ions over a small portion of the substrate that was defined by use of an appropriate mask.

The potential benefits of the ion-implanted semiconductor technology are the same as the optoelectronic advantages presented by LT-GaAs, and thus they apply both to civilian and Air Force needs. This means that improvements should be realized in the development of ultrafast sampling gates and the instruments that could benefit from their use. These include optoelectronic oscilloscopes and time-domain reflectometers that are based on fast photoconductive sampling and that could enhance temporal resolution to the one-picosecond regime. Applications also include antenna substrates for systems that generate and characterize subpicosecond electromagnetic pulses in terahertz-beam spectroscopy, radar, and imaging systems. Ultrafast photoconductive switches based on the implanted materials may also be used as subpicosecond pulse generators in order to produce test signals that could be used to test other terahertz electrical devices, transmission lines, and circuits.

### III.A.4 Femtosecond NSOM

Concurrently with the AFOSR-supported program summarized in this final report, we carried out a program on the development of a femtosecond near-field scanning optical microscope (NSOM) for the investigation of carrier dynamics in semiconductors with simultaneous high spatial and temporal resolution. That work was principally supported by NSF through the Center for Ultrafast Optical Science, but some materials and supplies support for this work was provided by this AFOSR program. One of the goals of the NSOM program has been to locally probe the dynamics of electrons around defects – a subject central to our AFOSR-supported work. By probing with simultaneous high spatial and temporal resolution, *local* carrier cooling, transport, and trapping properties could be measured directly, shedding light on their relationship to the microstructure in different materials. Variations in local impurity concentrations, defects, surface fields, and compositional changes should in principle affect carrier dynamics in bulk materials.

The first step in making these kinds of measurements was to characterize the measurement technique. We have reported the details of the development of the femtosecond NSOM and its initial application to the carrier dynamics in GaAs in [Smith 1998], and we refer the reader to that publication for a complete discussion. More complete details may be found in Smith's PhD thesis [Smith 1996].

A schematic diagram of the femtosecond NSOM developed in our laboratory is shown in Fig. 11. Pulses from an 80-fs Ti:sapphire oscillator were injected into an optical fiber after initially passing through a grating pair which pre-compensates the dispersion in the fiber. Thus the pulse duration at the fiber output was 80-fs. Ultrafast temporal resolution was made possible by splitting the pulse into two, with a variable delay between them, before injecting them into the fiber, enabling pump-probe type experiments to be performed. Since the two pulses were of equal energy and co-propagated in the fiber, the form of the pump-probe experiment was "equal-pulse correlation" as first implemented by Tang and coworkers [Tang 1983].

The output tip of the fiber was formed into a taper, which was then coated with approximately 100 nm of aluminum except for a small (200-nm) aperture at the output. The fiber was mounted in a piezoelectric tube, and the tip was held at a constant distance of about 5 nm from the sample surface using the technique of optically-detected shear-force feedback; this maintained the sample within the near field of the aperture. The sample was mounted on a piezoelectric tube which allowed the sample to be independently scanned underneath the fiber tip. The shear-force feedback signal was used to acquire a topographic image of the sample simultaneously with the optical image. This enabled us to distinguish the desired optical signals, which were due to bulk (subsurface) defects in semiconductor samples from those arising from topographical features such as dust, surface scratches and pits, etc.



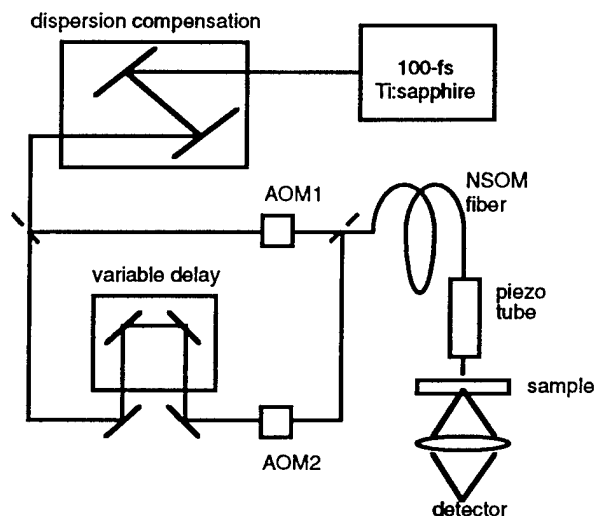


Figure 11. Schematic diagram of femtosecond NSOM experiment.

Femtosecond time resolution was obtained using the equal-pulse correlation technique. The signal in such an experiment was basically the convolution of the optical pulse autocorrelation with a double-sided exponential, where the exponential corresponds to the hot carrier relaxation. Thus the femtosecond NSOM experiment as implemented here basically measured local variations in the carrier relaxation rate (which were, of course, expected to be faster near defects, where trapping contributes to the overall relaxation rate). For very small NSOM apertures and early time delays, we expected that carrier transport, particularly the ballistic drift of electrons, would also contribute to the observed dynamics when the laser was tuned to photoinject carriers with significant initial kinetic energy. Our experiment showed preliminary evidence for such an effect. Figure 12 shows the time-resolved equal-pulse correlation signal for both normal MBE-GaAs and LT-GaAs with an excitation wavelength of 800 nm. Although far-field time-resolved measurements showed that the initial carrier relaxation was faster in LT-GaAs than it was in normal MBE-GaAs, the near-field measurements showed that the initial decay of the pump-probe signal was *faster* in MBE-GaAs than it is in LT-GaAs. This was contrary to what one would expect if only hot carrier relaxation contributed to the signal decay. Ballistic transport of hot carriers from underneath the NSOM tip, however, may also have contributed. For an excitation wavelength of 800 nm, the initial kinetic energy of the electrons is about 130 meV, which corresponds to a mean velocity of nearly  $10^8$  cm/s. Thus the mean escape time for ballistic electrons to leave the region underneath the aperture would be about 100 fs, consistent with what was observed in the normal MBE-GaAs. On the other hand, the strong momentum relaxation that will occur in the LT-GaAs due to the high defect density will suppress the ballistic transport, and carriers will transport out of the photoexcited region only by diffusion, which is on a much longer time scale. *Thus our experiments provided*

*preliminary evidence that time-resolved NSOM was a novel way to study ballistic transport of photoexcited carriers in semiconductors.*

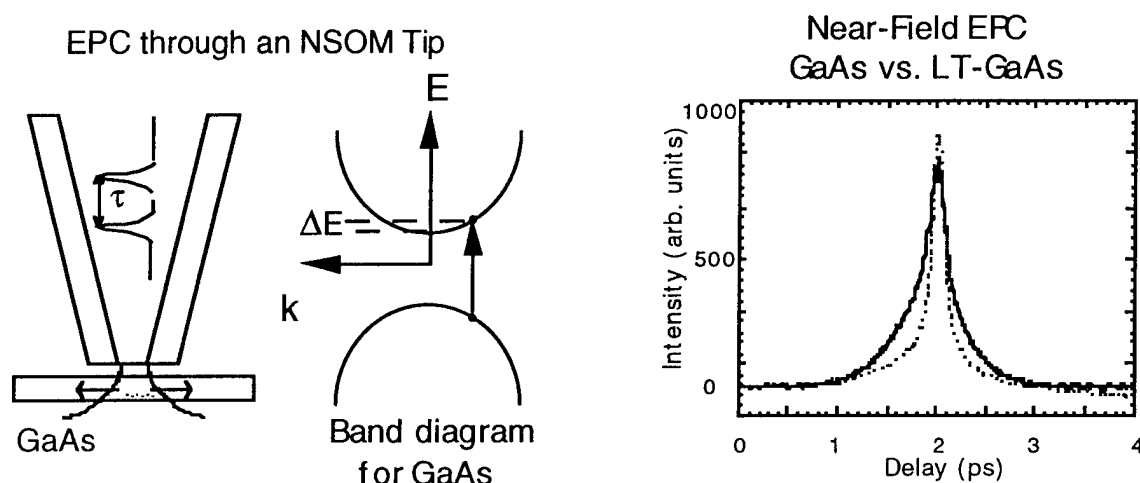


Figure 12. On the left is a schematic of the equal-pulse correlation measurement in GaAs, showing how carriers are photoinjected into a localized region of the semiconductor immediately below the NSOM tip. On the right is a comparison of the time-resolved signal for both normal MBE-grown GaAs and LT-GaAs.

Spatially and temporally resolved images of carrier dynamics near defects in GaAs are shown in Fig. 13. The images correspond to the equal-pulse correlation signal amplitude at different time delays. The sample was a 1-micron MBE-GaAs layer, and the laser wavelength 800 nm. As is explained further in [Smith 1998], the signal was actually sensitive only to defects within about 200 nm of the surface due to the reduced depth of field in the nonlinear NSOM signal. In the images, the overall signal amplitude was largest at time delay  $t=0$ , and decreased for times away from zero. In fact, the temporal dynamics may be measured at any specific location on the sample by fixing the NSOM tip at that location and taking a time scan. Inspection of the images showed that there were significant variations of the signal on the micron and submicron length scales. Several  $\sim 0.5 \mu\text{m}$  size regions of lower signal could be seen to correlate directly with topography, demonstrating the shallow depth of field in this measurement. Several regions of higher intensity which did not correlate with the topography could be seen in the images, the smallest of which were  $\sim 200 \text{ nm}$  FWHM. An increase in the nonlinear response could arise from variations in carrier cooling or conduction-band lifetimes caused by the presence of impurities or nonstoichiometric precipitates. An order-of-magnitude calculation using the images and the depth of field estimates yielded a defect density of  $10^{13} \text{ cm}^{-3}$ , which was not unreasonable at the surface of an MBE-grown film. While the origin of these regions of larger nonlinear signal cannot be determined by these optical experiments, in the future the

## EPC in GaAs Spatially Resolved

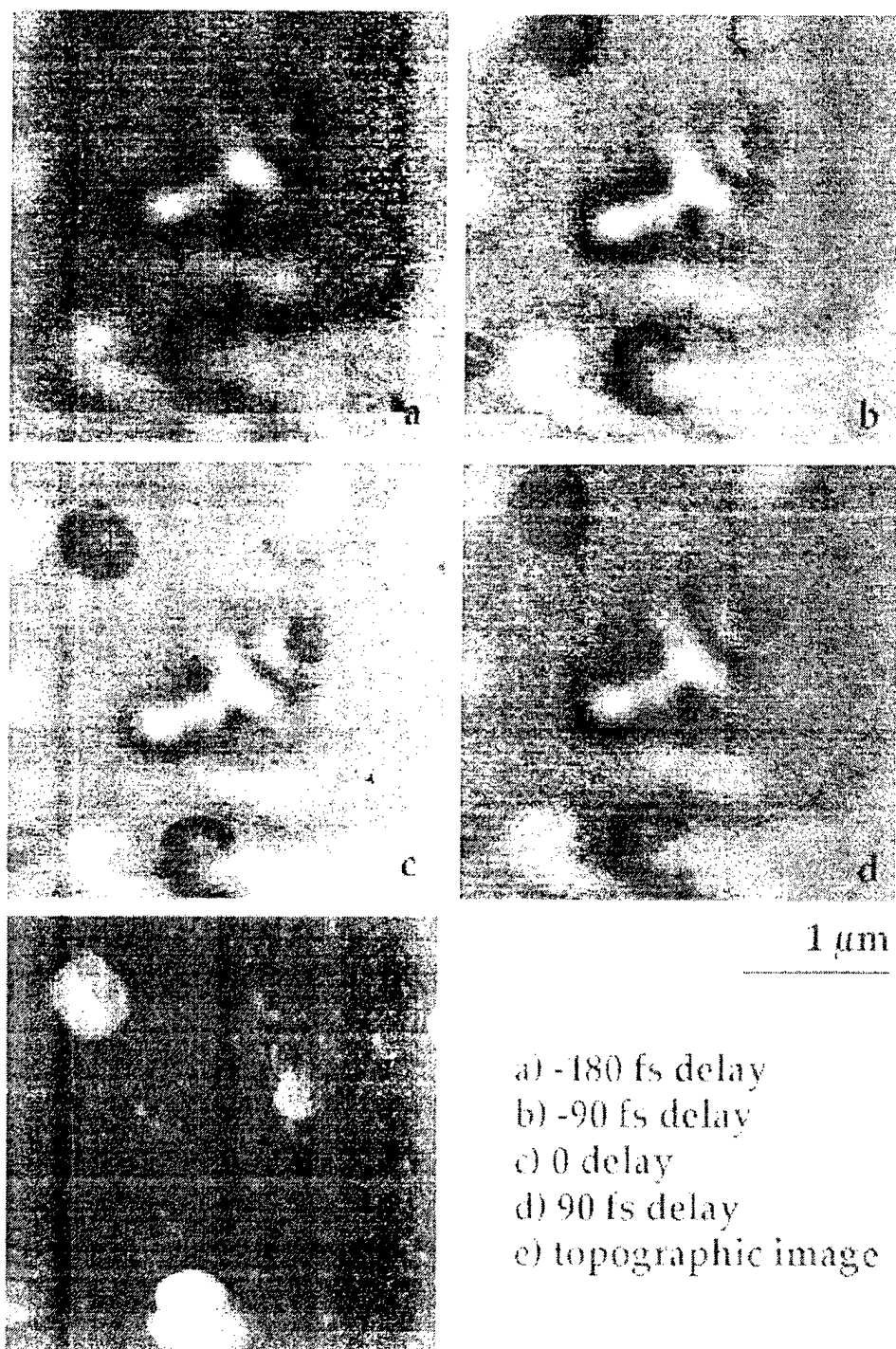


Figure 13. Images (a-d) show the nonlinear equal-pulse correlation signal in GaAs for different time delays. The bright areas correspond to near-surface defects; assuming the defect size to be smaller than the NSOM aperture, the spatial resolution of the system is seen to be about 200 nm. Image (e) is the simultaneously acquired topographic image.

optically-measured carrier dynamics could be correlated with other defect characterization techniques to provide more complete information on the effect of specific defects on carrier dynamics.

### *III.B. Photoconductive Probe Development*

As mentioned above, the unique combination of properties exhibited by the nonstoichiometric LT-grown and annealed GaAs layers – high resistivity, ultrashort carrier trapping time, high breakdown voltage, and high mobility – have made them the best choice to date for use as the active material in ultrafast optoelectronic devices. In tandem with the development of fast photoconductive switches and detectors (often called Auston switches), we have, under AFOSR support, also pioneered the use of LT-GaAs in the complementary application of fast gating or sampling of electrical signals.

The most advanced embodiment of these so-called photogates is a micromachined, optical-fiber-mounted, active sampling head (Fig. 14). This device consisted of a 1- $\mu\text{m}$ -thick epitaxial lift-off layer of LT-GaAs that was attached along the side of a single-mode optical fiber with transparent, ultraviolet-curing cement. The fiber was polished at a 45° angle at its end, so that the laser pulses guided by the fiber were reflected via total internal reflection onto the LT-GaAs. The metal pattern on the LT-GaAs had an interdigitated region that was 30 x 30  $\mu\text{m}$  in area, with 1.5- $\mu\text{m}$  finger widths and gaps. This high-resistance area of the probe transitioned down to a 7- $\mu\text{m}$ -wide tab that extended out past the end of the LT-GaAs (in a similar fashion as a diving board) and acted as the contacting probe tip. The other end of the probe had a flared metal tab that was contacted to silver epoxy that coated the outside of the optical fiber. When the probe tip senses a potential on an interconnect, there is also a potential drop across the interdigitated region, and when the laser pulses generated carriers in this region, they drifted and gave rise to a photocurrent that was proportional to the bias potential. These sampled current signals were then transmitted from the probe using the conductive epoxy on the fiber.

The true utility of the photoconductive (PC) probe arises from its high impedance, low invasiveness and extremely high voltage sensitivity [Lai 1996]. These properties were not inherent in the PC probe itself, but rather were dependent on the presence of a follow-on “amplifier,” which is actually a source follower [Hwang 1996a]. While a good deal of the initial development for the PC probe actually took place under the auspices of other support before this AFOSR contract commenced, the key advantages of the probe were only realized after the integration of the probe with the source follower as a part of the AFOSR-sponsored program. The impact of the source follower is described in the first subsection, followed by several subsections that present applications of the PC probe for electronics and pulsed terahertz beams.



Figure 14. Photomicrograph of photoconductive probe sampling head.

### III.B.1 Ultrafast Photoconductive Voltage and Field Probing

The principle drawback to the photoconductive sampling process, and the one that had historically limited the voltage sensitivity of photogate measurements to  $> 1 \mu\text{V}/\text{Hz}^{0.5}$ , was that the resulting photocurrent coming from the sampling gate had typically been deposited on the capacitance of the output coaxial cable and the instrumentation to which the cable led. As a part of our AFOSR program, we have found that the introduction of the source follower immediately at the output of the optical fiber leading from the PC probe has effectively solved this problem by dramatically decreasing the capacitance to be charged by the sampling photocurrent. This, in turn, has enhanced the applicability of the PC probe by not only making it more sensitive to smaller potentials, but also by decreasing data acquisition times for larger signals and by allowing the absolute voltage levels of signals to be sensed.

As the first step, the PC probe head was integrated in a hybrid configuration with a pair of matched JFETs that acted as a source-follower/amplifier (SF/A) or buffer. An equivalent circuit of the PC probe head and the source follower are shown in Fig. 15. With this SF/A circuit and the ultra-high input impedance of the JFETs, the LT-GaAs probe was converted from a device that sensed current to one that sensed voltage. Subsequently, we were also able to experimentally demonstrate that the inclusion of the SF/A improved the performance of an LT-GaAs photoconductive-sampling probe over 100 times in regard to invasiveness and gating efficiency, while maintaining a 1-ps temporal response and enhancing the signal-to-noise performance of a probe. Laser powers as low as  $10 \mu\text{W}$  were proven to be sufficient for driving the photogate, and the requirement that an external current preamplifier or a lock-in amplifier be used to achieve acceptable signal-to-noise ratio was eliminated.

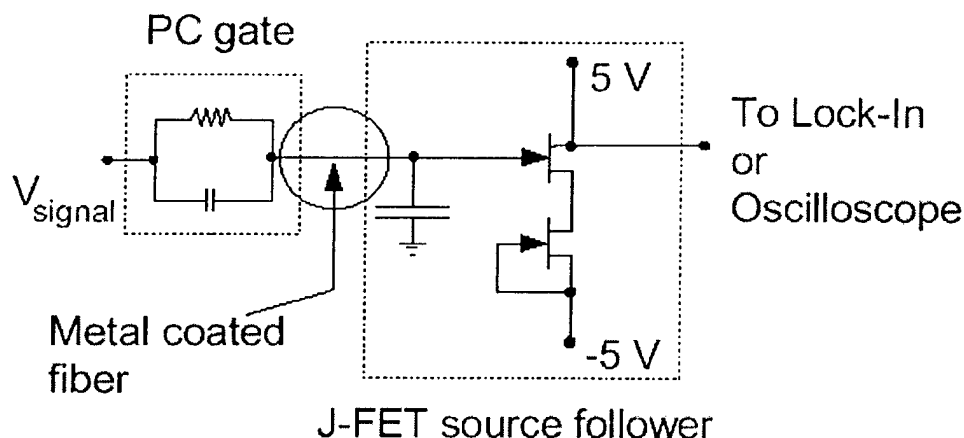


Figure 15. Equivalent circuit of the photoconductive sampling head integrated with a source follower.

The most dramatic improvement demonstrated in the LT-GaAs photoconductive sampling probes with the JFET buffer was in the voltage sensitivity. Sampling circuits had been limited to a resolution of several  $\mu\text{V}/(\text{Hz})^{1/2}$  primarily due to photovoltaic noise from laser-pulse amplitude fluctuations. However, the integration of the source follower reduced the output capacitance of the sampling gate by nearly two orders of magnitude (from typically 200 pF to 3 pF) and also increased the effective impedance seen by the sampled electrical signal to  $> 1 \text{ T}\Omega$ . This allowed us to increase the frequency of modulation used with phase-sensitive detection and thus to reduce the  $1/f$  gate noise to the extremely low level of  $15 \text{ nV}/(\text{Hz})^{1/2}$  [Hwang 1996b].

The signal-to-noise ratio (SNR) of LT-GaAs photoconductive sampling-probe measurements was also raised appreciably with the use of the source follower. Without the source follower, the SNR of our LT-GaAs sampling circuit was limited by the small modulation bandwidth that was required when the large external parasitic capacitance was present (Fig. 16, open circles). The SNR varied little with modulation frequency, since the signal and noise both had a  $1/f$  frequency dependence. With the source follower, higher modulation frequencies were possible, and since there was also decreased leakage current because of the huge JFET input impedance ( $\gg 10$  times larger than the dark resistance of the LT-GaAs gate), the same 1.4 mW of gating laser power that illuminated the unamplified probe led to a SNR improvement of more than 50 for the amplified probe at a 50 kHz modulation frequency (Fig. 16, filled squares). The total SNR for this amplified PC probe was extended out to 300.

The high sensitivity of the PC sampling head has also led to its application in a field-sensitive photoconductive sampling technique that measures signals through insulating passivation layers without the need for conductive contact or charge drainage [Hwang 1996c]. To demonstrate such measurements, the fiber-mounted LT-GaAs probe was first brought into

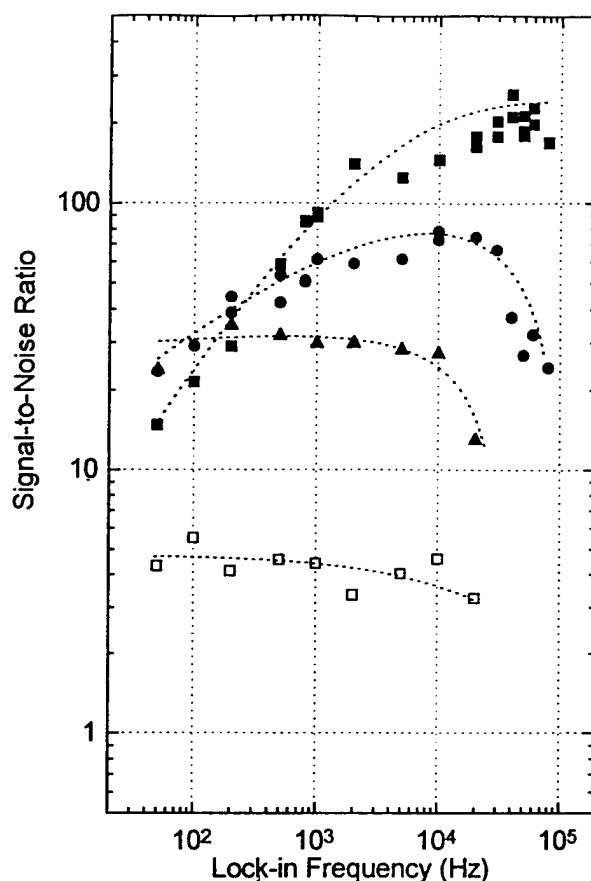


Figure 16. Signal-to-noise ratio: LT-GaAs photoconductive probe with (solid symbols) and without (open symbol) source follower. Gating laser intensities: square, 1.4 mW; circle, 100  $\mu$ W; triangle, 10  $\mu$ W.

contact with a 4000-Å-thick passivation layer of  $\text{SiO}_2$  that had been deposited over the two electrodes of a coplanar stripline (CPS), and a short pulse was launched onto the CPS. Since the dimensions of the metal ribbon tip were much larger than the thickness of the passivation layer, the tip could be considered as a parallel plate capacitor with a capacitance of about 12 fF. When the metal ribbon tip had no *conductive* contact to the DUT, it was essentially a floating metal line with a high-impedance photoconductive switch at its opposite end. Furthermore, the LT-GaAs photoconductive gate was also floating, but virtually grounded by the  $> 1 \text{ T}\Omega$  input impedance of the integrated source follower/amplifier.

In principle, the launched signal traveling along the CPS behaved as a sheet-charge-density wave passing the floating probe. An image sheet-charge-density wave with the same magnitude but opposite polarity was then induced on the floating probe tip due to its proximity. Similarly, a reverse sheet charge density was induced at the photogate and, after another reversal, again at the source follower capacitance. A differential induced voltage was then sensed by the source follower when the LT-GaAs gate was closed by the gating laser pulses. The minimum

detectable voltage in this probe configuration was determined to be  $2.5 \mu\text{V}/(\text{Hz})^{1/2}$ , or approximately 100 times smaller than signals measured through passivation layers by other techniques.

The LT-GaAs photoconductive sampling circuit was also used without the source follower in a configuration that demonstrated its utility as an efficient picosecond waveform launcher. With a second photoconductive element acting as an amplified sampling gate, the output of the switch/launcher was measured with the metal tab contact tips placed  $15 \mu\text{m}$  apart on a grounded metallic line. The correlation waveform of the two probes was found to have an observed FWHM of 5 ps (Fig. 17). The reflections observed in the signal following the main pulse of the transient were not unexpected due to the various impedance mismatches present in the experimental geometry. This application of the PC probe as a freely-positionable pulse generator also led to an investigation of the usefulness of the probes as pulsed-terahertz transmitters.

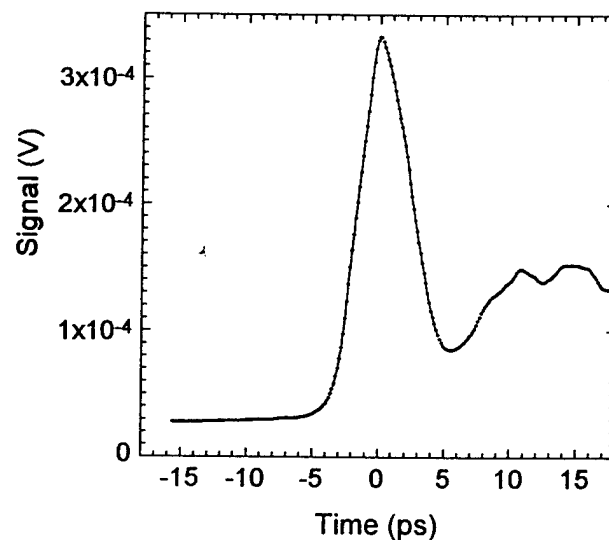


Figure 17. Waveform generated with LT-GaAs photoconductive launcher.



### III.B.2 Miniature THz Source

A micromachined THz emitter was produced using similar fabrication techniques as those employed for the PC probe. A pair of single-mode optical fibers were glued onto the emitter using ultraviolet-curing cement. As for the PC probe, one of the fibers was polished with a  $45^\circ$  bevel to allow the guided laser pulses to internally reflect off the core surface to the backside of the emitter and into the interdigitated photoconductive switch. The other fiber provided only mechanical stability and provided a means to position the emitter. A top view of the THz emitter is shown in Fig. 18.

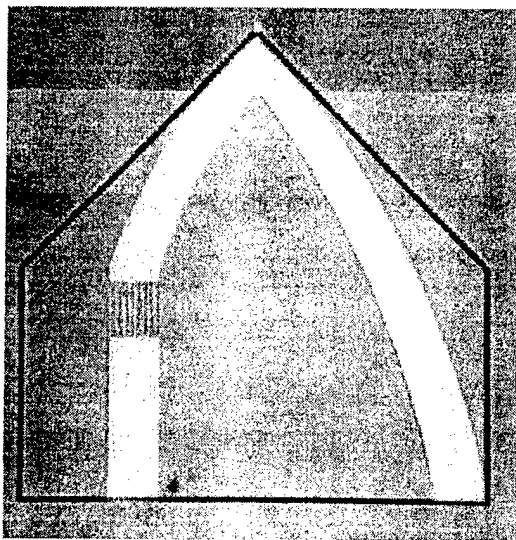


Figure 18. Photomicrograph of the THz emitter before liftoff from the GaAs substrate. The left electrode was connected to a dc voltage source while the right electrode was connected to ground.

The THz radiation from the emitter was measured using a PC probe, positioned with its tip in contact with a long, narrow grounded line, as the receiver (shown in Fig. 19). As described earlier, the output of the PC probe was connected through a source follower to a lock-in amplifier. The emitter electrode leading to the PC switch was biased with a 5-V dc supply, while the other electrode on the emitter was grounded. The relative electric field of the radiated signal was measured by reading the lock-in amplifier at different delay times between two separate laser pulse trains used to trigger the emitter and receiver.

The signals that were measured were found to contain contributions from both electric and magnetic dipoles. In certain directions (*i.e.*, in the plane), the magnetic component dominated. For instance, Fig. 20(a) shows a temporally resolved waveform generated by the emitter when it was located  $500\text{ }\mu\text{m}$  away from the PC probe in the x direction (see axes in Fig. 19). The strong lateral radiation of the new emitter was unusual for THz signal sources, which

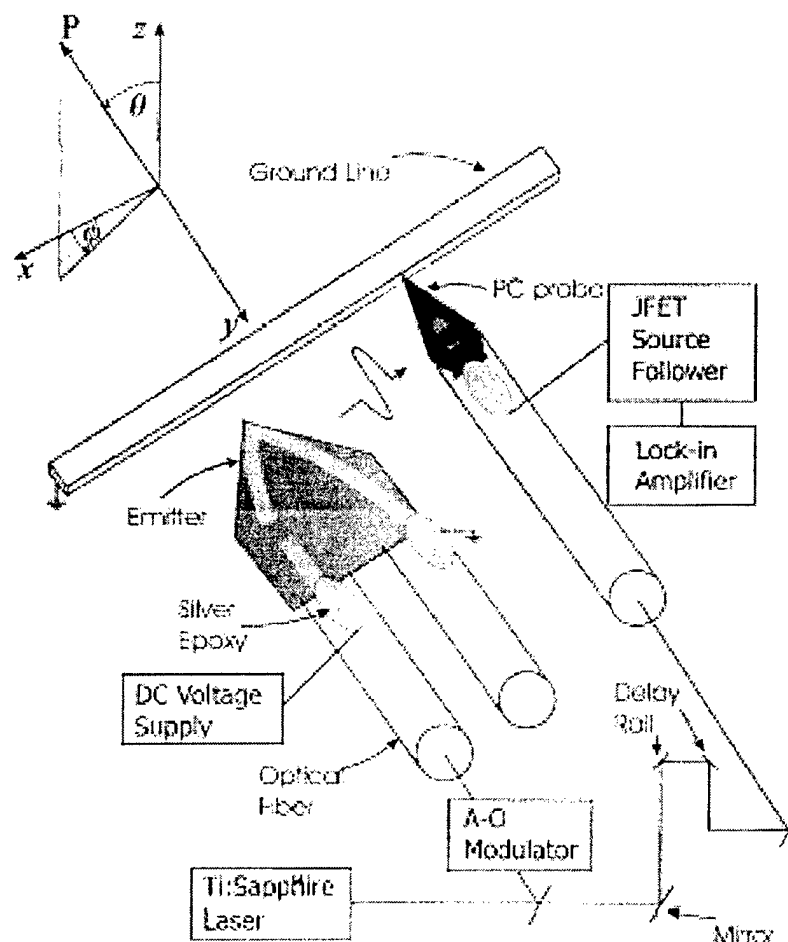


Figure 19. Experimental setup with the fiber mounted emitter and PC probe acting as a terahertz receiver.

typically radiate a signal from a transient electric dipole created between the two electrodes of a PC switch. In Fig. 20(b) electric dipoles were formed between the tips of the interdigitated fingers and the bases of the other electrode (see the figure caption for an explanation of the position of the receiver). However, most of the radiation detected in Fig. 20(a) was produced by a transient magnetic moment because the semilooping structure behaved as a magnetic dipole, allowing radiation to be transmitted planar to the PC switch area. Signals were also compared at two positions in the plane of the emitter on opposite sides of the PC switch. Figure 20(a) shows the signal when the PC probe was placed 500  $\mu\text{m}$  away from the ground-electrode side of the emitter. Figure 20(c) shows the signal when the PC probe was positioned 500  $\mu\text{m}$  away from the PC switch side of the emitter. The opposite polarities of the measured waveforms further confirmed that the radiation was mostly due to the magnetic dipole, since the field was in the  $-\phi$  direction in the x-y plane.

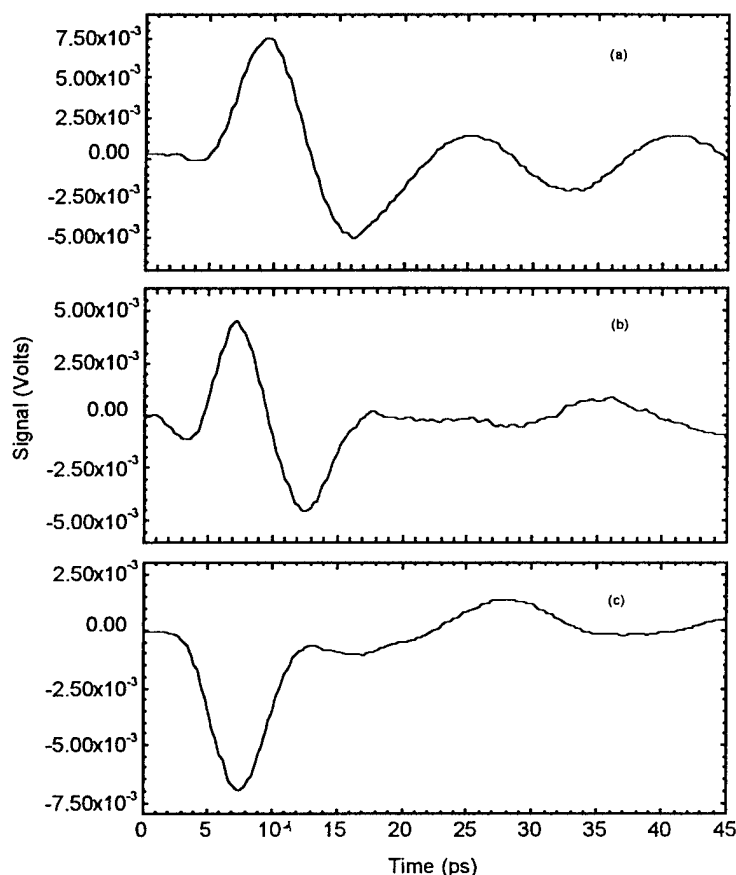


Figure 20. Temporally-resolved waveforms of the terahertz signal generated by the micromachined THz emitter. (a) Measurement made with the setup shown in Fig. 19 with the photoconductive probe 500  $\mu\text{m}$  away from the emitter in the  $-x$  direction. (b) Measurement taken with the photoconductive probe placed several tens of micrometers away from the emitter in the  $+z$  direction. (c) Measurement made with the photoconductive probe positioned 500  $\mu\text{m}$  away from the emitter in the  $+x$  direction.

A simple dipole model was used to explain the increased magnetic dipole radiation relative to the electric dipole. To summarize the results, for electric and magnetic dipoles of the same dimensions, the electric dipole radiation would typically dominate. However, as the size of the magnetic dipole becomes significantly larger, as in the case of our emitter, the magnetic dipole contribution becomes important.

The micromachined, freely-positionable emitter featured a small area of 300  $\mu\text{m}$  by 300  $\mu\text{m}$ , with a photoconductive switch area of 30  $\mu\text{m}$  by 30  $\mu\text{m}$ . This compact geometry, coupled with the fact that no other bulk optics were required for optical manipulation, suggests applications for the emitter in terahertz, time-domain, near-field spectroscopy and imaging.

### III.B.3 Applications to Device and Circuit Measurements

Besides its use in the characterization and generation of guided and free-space electrical transients, the PC probe has also been applied extensively as a unique diagnostic tool for microwave analog and digital circuits. The novel way in which the probe has been used to extract signals from within circuits will first be explained, and then some examples of results will be provided.

Since the analog input for an MMIC or the clock input for a microwave digital circuit are repeating, continuous waveforms, it was necessary to devise a new means for executing a time delay between the probe laser pulses that triggered the PC sampling gate and the continuously varying waveforms to be measured. The techniques of heterodyne mixing and equivalent-time sampling were chosen to accomplish this. If the unknown signal is repeating at a frequency  $f_m$ , where  $f_m$  is given by

$$f_m = n \cdot f_{rep} \pm f_{IF}$$

and  $f_{IF}$  is an intermediate frequency (e.g., in the kHz-range, also called modulation frequency),  $n$  an integer number and  $f_{rep}$  the repetition frequency of the sampling gates, then the signal will be sampled with the frequency  $f_{IF}$ , and a downconverted replica will appear at this frequency.

A block diagram of the system configuration, which includes the sources and locations of the mixing-frequency components, is shown in Fig. 21. The probe was in conductive contact with a circuit internal node, where the unknown signal was to be measured. A train of femtosecond-duration laser pulses illuminated the probe, and its output voltage was recorded on a low-frequency electronic measurement instrument, such as an oscilloscope, making the temporal waveforms at the intermediate frequency accessible. A lock-in amplifier or a spectrum analyzer could also be used to display the amplitude and phase of  $f_{IF}$  and its harmonics, so that the unknown microwave signal could be determined in the frequency domain.

The positioning of the 7- $\mu\text{m}$  wide metal tip determined the spatial resolution of the probe used. This probe tip was sufficiently small that we could interrogate interconnects in many microwave circuits, even with features much smaller than 1  $\mu\text{m}$ . It should be mentioned that decreasing the probe tip width could easily increase the resolution further, or a fine conical tip could be employed to access the sub- $\mu\text{m}$  regime. To demonstrate the limit for the resolution of the probe, a transmission line with a width of 5  $\mu\text{m}$  was used as a DUT. The probe was translated transverse to the biased line using a high precision translation stage (100 nm minimal incremental motion) while the probe output voltage was measured. The minimal overlap between the metal line and the probe tip that was required to still measure the absolute voltage on the

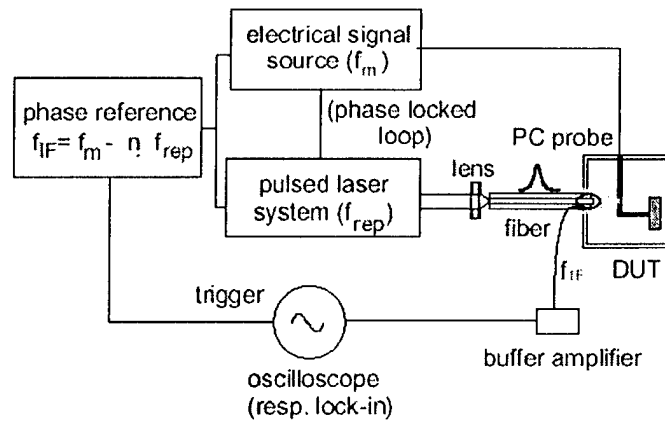


Figure 21. Experimental setup for circuit measurements using the photoconductive probe.

transmission line was determined to be about 400 nm. Thus, even circuit nodes with sub- $\mu\text{m}$  structure size would be accessible by the probe tip, if the traces in a circuit were not packed too densely that the probe would overlap multiple lines and short them.

As a first example, a high speed, InP heterojunction bipolar transistor (HBT) frequency divider was examined using the PC probe. The circuit provided a differential divide by four output based on a differential input clock, and it was nominally designed to operate at 3.5 GHz. Internal dividers were based on latches constructed using differential pairs, where current was steered from one branch of the differential pair to the other to effect a change of logic state. The layout (Fig. 22) and the block diagram (Fig. 23) of the circuit are annotated to show some of the probing locations. The device as configured was operated single-endedly, with one side of the

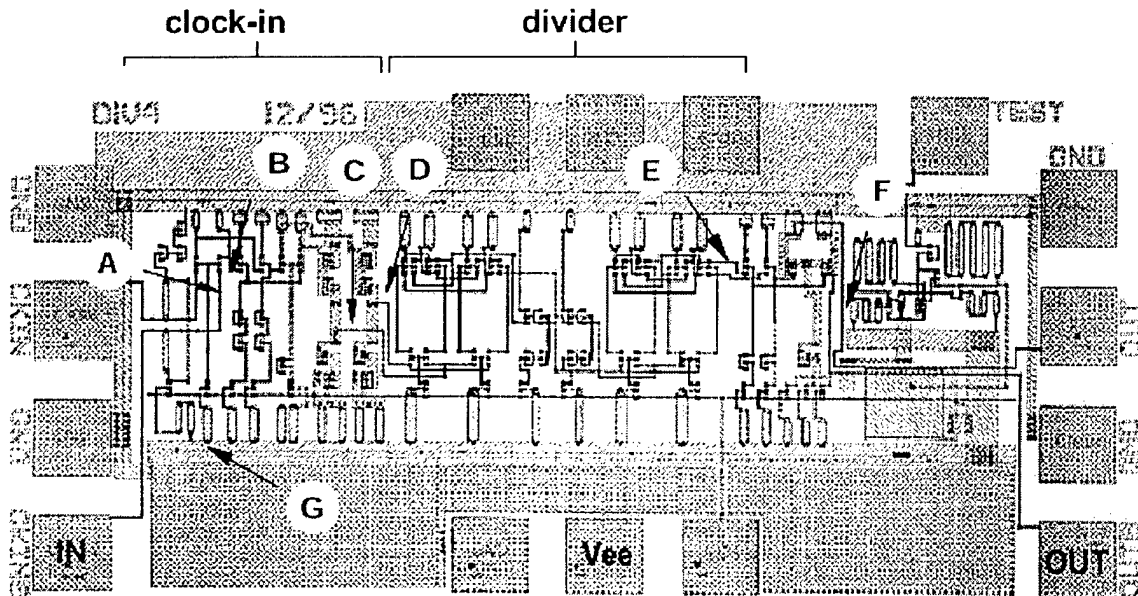


Figure 22. Investigated InP frequency divider circuit with locations of probed nodes marked.

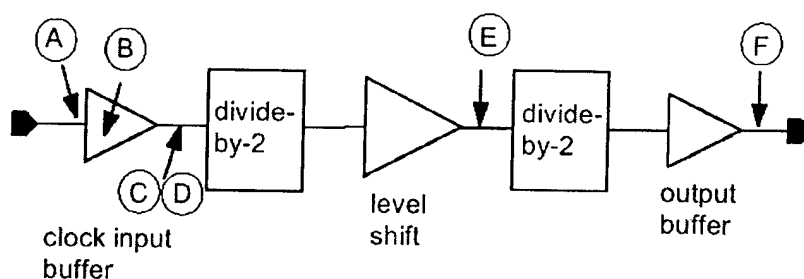


Figure 23. Block diagram of example digital circuit.

differential input floated to its threshold. The single-ended input was ac-coupled with dc biases set by internal circuit nodes.

Internal node measurements from the circuit were performed at frequencies up to 16 GHz, although the examples shown here were acquired at a clock of 10.56 GHz. The single-ended input was probed at location (A) in Figs. 22 and 23. The 10.56 GHz sinusoidal input shows both the internal dc level of -2.2 V and an input swing of 700 mV peak to peak (Fig. 24[a]). This value is consistent with an attenuation of 7 dB due to the connecting microwave cable and dc blocking capacitor (applied output power of the synthesizer was 6 dBm). Position (B), as shown on the layout in Fig. 22 and 23, yielded a waveform that illustrated how the collector of the differential amplifier circuit operated single-endedly, where one differential pair transistor acted as an emitter-follower and the other was cut off (Fig. 24[b]). This caused a distortion of the sinusoid at that location. The ac component is 350 mV and the dc level is -0.2 V. Note that a 7.1 ps propagation delay is measured between positions (A) and (B) corresponding to the expected transistor delay (after taking into account that the collector output (B) is inverted with respect to the emitter input (A)).

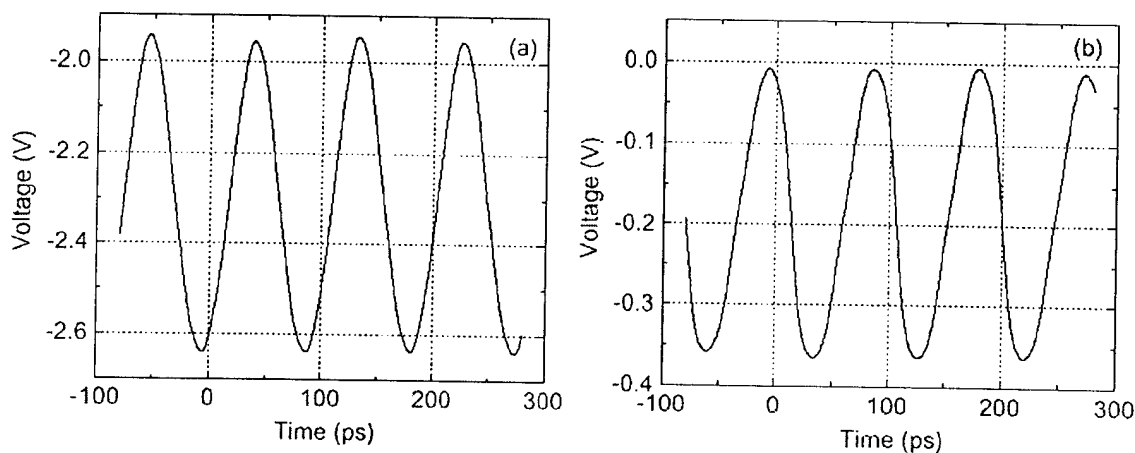


Figure 24. Sinusoidal microwave input of 10.56 GHz, (a) measured at position (A), (b) measured waveform at position (B)

The differential output of the input clock buffer was probed at locations (C) and (D). The results for the true input buffer output and its complement displayed phase inversion between the complementary outputs and the dc levels was as expected. Two cascaded divide-by-two circuits created the divide-by-four function. Figure 25 shows the second stage divide-by-two output probed at position (F) on the layout, revealing a frequency of 2.64 GHz (10.56 GHz/4). The non-sinusoidal waveform indicated the presence of higher harmonics. When the circuit was operated at lower frequencies, for instance at its design frequency of 3.5 GHz, the higher harmonics completely transform the sinusoids to square waves.

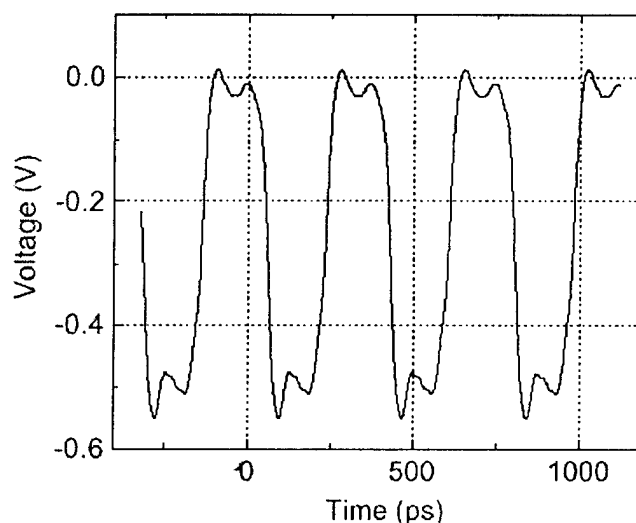


Figure 25. Output signal of the second divide-by-2 at pos. F (note the extended time axis).

The probing of the internal node waveforms of a microwave frequency divider circuit operating at a frequency of 10.56 GHz have demonstrated the characteristic operation of the circuit (e.g., gate delays, frequency division and power bus noise [not shown]). The results demonstrated that the PC probe has a broad potential as a diagnostic tool, particularly for digital circuits as they push up towards millimeter-wave operating frequencies. Furthermore, the probe should also provide a novel capability for validation of circuit models as they become increasingly complex and cover higher frequencies of operation. This is also true for analog, or monolithic microwave ICs, as will be demonstrated now.

This second example of the application of the PC probe for internal circuit-diagnostic applications investigated a three-stage amplifier based on Si/SiGe HBTs and micromachined lumped elements as matching elements (Fig. 26). The circuit was found by conventional network

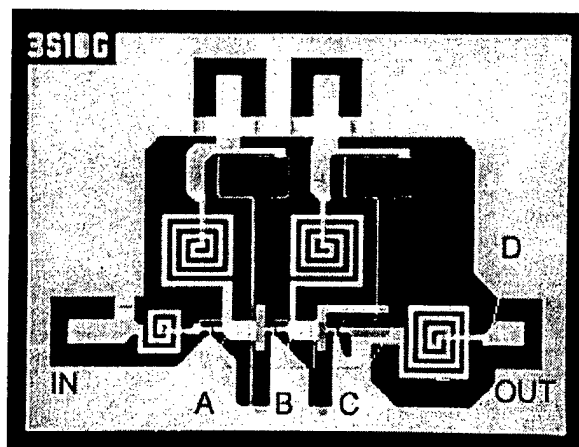


Figure 26. Three-stage SiGe amplifier, chip size: 1.15 x 0.84 mm; measured nodes are marked A-D.

analysis to have a maximum gain of 12.6 dB at 11.1 GHz, as measured through an on-wafer probe at the end of the third stage. Figure 27 displays this result, as well as a simulation result obtained using HP EEsof's LIBRA 5.0. A good agreement was observed between the network analyzer and LIBRA results, especially near the design frequency at approximately 10 GHz. A second measurement of the circuit performed approximately 6 months after the processing revealed a degradation of the circuit performance. At this time, the amplification was determined to be only 7 dB, with the degradation likely occurring because of excessive bias applied to the circuit during additional measurements. Figure 28 shows the gain of the circuit as determined both by the second network analyzer measurement (of the circuit after degradation) and by the photoconductive measurement. A very good agreement was observed in this comparison, providing strong evidence of the high degree of accuracy that could be expected from the photoconductive probe measurements.

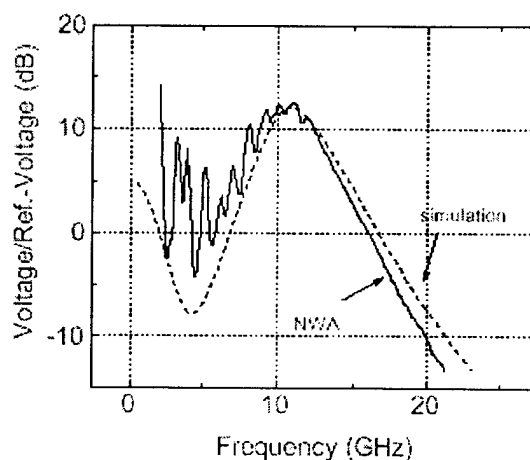


Figure 27. Network analyzer (NWA) measurement and simulation of 3-stage amplifier gain.



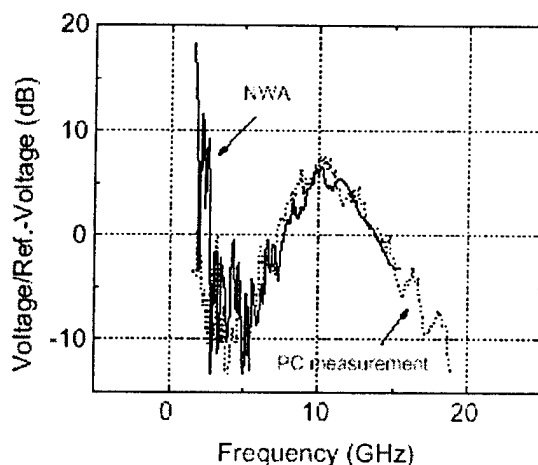


Figure 28. Results of NWA measurement ( $S_{21}$ ) and photoconductive-probe measurement of the output of the circuit at position D.

The potentials at the circuit's interior were also determined using HP EEsof's LIBRA 5.0. In order to accomplish this, test points were inserted at the circuit nodes, and the potentials were calculated using the harmonic balance method. Since LIBRA accurately simulated the output of the circuit as it operated originally, and we could reasonably assume then that it also simulated the correct response at the circuit internal test points when the circuit was initially fabricated, we used comparisons between the PC probe measurements and the LIBRA simulations to determine how the internal circuit characteristics changed. These measurements then also revealed which amplifier stages were responsible for the degraded performance.

The spectra obtained at the internal nodes A-D both for the simulations and measurements corresponded to the sum of the potentials of the forward and backward propagating waves at the nodes. The shapes of the spectra agreed very well, showing the maximum amplification at 10.5 GHz for the photoconductive measurement results and 10.8 GHz for the simulation. However, there was a discrepancy in the absolute value of around 5 dB for all of the measurements across much of the measured frequency range. This is illustrated in Fig. 29, where a difference between the simulated and measured signals of 5 dB at the operating frequency is obvious at the output of the first stage (A). It is important to note that this difference virtually does not change at 10 GHz as the signal passes through the second and third stages (B and C). Thus, this result implies that the first stage had the greatest impact on the actual performance of the circuit, as it degraded from the simulated performance. In fact, the PC probe measurement confirmed that the second and third stages were exhibiting their expected performance.

It should also be noted that, just as for conventional network analysis, it was necessary to perform a calibration procedure for these frequency-domain measurements. This is described in [David 1998], but it can be mentioned that the PC probe calibration should be somewhat less complicated than the calibration for conventional network analysis based on the fact that the PC probe technique measures signals directly on the probe, before any cables and adapters.

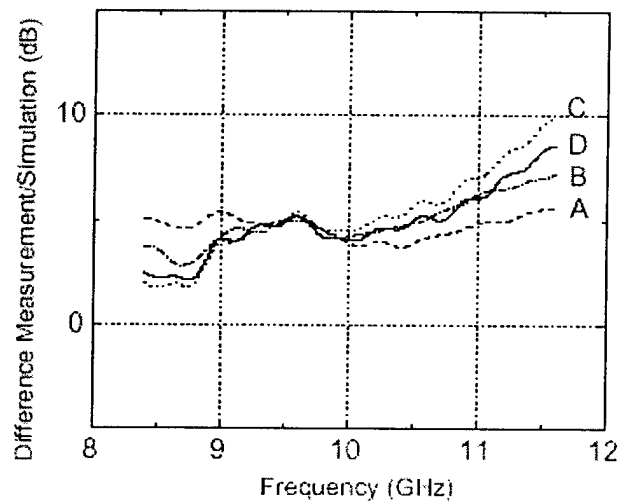


Figure 29. Difference between PC probe measurements and LIBRA simulation.

## References

- [Benjamin 1994] S. D. Benjamin, A. Othonos, and P. W. E. Smith, *Electron. Lett.* 30, 1704 (1994).
- [David 1998] G. David, T. Yun, M. Crites, J.F. Whitaker, T.R. Weatherford, K. Jobe, S. Meyer, M. Bustamante, W. Goyette, S. Thomas III, and K. Elliott, *IEEE Trans. Microwave Theory Tech.*, 46, 2330 (1998).
- [Hwang 1996a] J.-R. Hwang, H.-J. Cheng, J.F. Whitaker, and J.V. Rudd, *Appl. Phys. Lett.*, 68, 1464 (1996).
- [Hwang 1996b] J.R. Hwang, H.J. Cheng, J.F. Whitaker, and J.V. Rudd, *Optical and Quantum Electronics*, 28, 961 (1996).
- [Hwang 1996c] J.-R. Hwang, R.K. Lai, J. Nees, T.B. Norris, and J.F. Whitaker, *Appl. Phys. Lett.*, 69, 2211 (1996).
- [Jager 1993] N. D. Jager, A. K. Verma, P. Dreszer, N. Newman, Z. Liliental-Weber, M. van Schilfgaarde, and E. R. Weber, *J. Electron. Mater.* 22, 1499 (1993).
- [Kaminska 1989] M. Kaminska, E. R. Weber, Z. Liliental-Weber, R. Leon and Z. Rek, *J. Vac. Sci. Technol.* B7, 710 (1989).
- [Lai 1996] R.K. Lai, J.-R. Hwang, J. Nees, T.B. Norris, and J.F. Whitaker, *Appl. Phys. Lett.*, 69, 1843 (1996).
- [Look 1993a] : D. C. Look, *Thin Solid Films* 231, 61 (1993).
- [Look 1993b] D. C. Look, G. D. Robinson, J. R. Sizelove, and C. E. Stutz, *J. Electron. Mater.* 22, 1425 (1993).
- [Siegnier 1996] U. Siegnier, R. Fluck, G. Zhang, and U. Keller, *Appl. Phys. Lett.*, 69, 2566 (1996).
- [Smith 1988] F. W. Smith, A. R. Calawa, C.-L. Chen, M. J. Manfra, and L. J. Mahoney, *IEEE Electron. Device. Lett.* 9, 77 (1988).
- [Smith 1996] S. Smith, PhD Thesis, The University of Michigan (1996).
- [Smith 1998] S. Smith, N.C.R. Holme, B. Orr, R. Kopelman, and T. Norris, *Ultramicroscopy* 71, 213 (1998).
- [Tang 1983] C.L. Tang, et al., *Phys. Rev. Lett.* 51, 844 (1983).
- [Tomassi 1995] R. Tomassi, P.L. Langot, and F. Vallee, *Appl. Phys. Lett.*, 66, 1361 (1995).

[Wang 1995] H.H. Wang, J.F. Whitaker, K. Al-hemyari, and S.L. Williamson, in *Defect and Impurity Engineered Semiconductors and Devices*, edited by S. Ashok, J. Chevallier, I. Akasaki, N.M. Johnson, and B.L. Soporì (Materials Research Society, Pittsburgh, 1995), pp. 1001-1006.

[Wang 1996] H. H. Wang, Ph.D. Thesis, The University of Michigan (1996).

[Warren 1991] A. C. Warren, N. Katzenellenbogen, D. Grischkowsky, J. M. Woodall, M. R. Melloch, and N. Otsuka, *Appl. Phys. Lett.* **58**, 1512 (1991).

[Whitaker 1993] J. F. Whitaker, *Mat. Sci. Eng.* **B22**, 61 (1993).

#### *IV. Interactions with DRET-Funded Program*

Our research program began in conjunction with a joint program in France funded by DRET and centered at the Condensed Matter Physics Laboratory at Ecole Polytechnique in collaboration with Daniel Kaplan of Alliage, Inc. and Thomson-CSF. The goal of that program was to investigate the physics of trapping and recombination in SI-GaAs, which is closely related to similar physics in LT-GaAs. As part of the collaboration between our laboratories, Kaplan made a number of visits to Michigan, spending a total of 16 weeks at the University to utilize the laser and microfabrication expertise supported by AFOSR. The work on the program in recombination physics has led to two major advances. First, a deeper understanding of recombination in SI-GaAs has enabled significant improvements in switching efficiency for high-voltage switches. This investigation of SI-GaAs has led in turn to revolutionary advances in streak camera operation (specifically, an increase in the repetition rate of picosecond-resolution cameras to >1 kHz from its current state of the art of 10 Hz). This work led to the development and commercialization of a high-repetition-rate averaging streak camera that requires a very low laser-trigger-pulse. The development of this instrument was carried out in a joint effort between Michigan and Alliage, in collaboration with Medox, Inc., an Ann Arbor company. Medox was recently bought by Thomson-CSF, which now markets the streak camera.

It is interesting to note that the joint research program has enabled significant, even orders-of-magnitude, improvements to photoconductive technologies for both high-voltage (kV) and ultra sensitive (nV) optoelectronic devices.

*V. Personnel Supported/Associated*

Directly supported:

Ted Norris	Co-PI (Assoc. Prof.)
John Whitaker	Co-PI (Scientist)
Hsi-Huai Wang	Graduate Student
Amy Raudenbush	Graduate Student
Richard Lai	Graduate Student
Tom Sosnowski	Graduate Student
John Om	Graduate Student
Junji Urayama	Graduate Student
Marni Arnett	Administration
Tammy Zill	Clerical
Martha Maxwell	Clerical
Faye Booker-Logan	Clerical

4

Associated:

Dr. Paul Grenier	Post-doctoral fellow
Dr. Gerhard David	Post-doctoral fellow
Jiunn-Ren Hwang	Graduate Student
C.-Y. Sung	Graduate Student
Joe Hayden	Graduate student

## VI. Publications

1. R.K. Lai, J.-R. Hwang, T.B. Norris, and J.F. Whitaker, "A Photoconductive Miniature Terahertz Source," *Appl. Phys. Lett.* **72**, 3100 (1998).
2. S. Smith, N.C.R. Holme, R. Kopelman, B. Orr, and T. Norris, "Ultrafast Measurements in GaAs Thin Films using NSOM," *Ultramicroscopy* **71**, 213 (1998).
3. G. David, T. Yun, M. Crites, J.F. Whitaker, T.R. Weatherford, K. Jobe, S. Meyer, M. Bustamante, W. Goyette, S. Thomas III, and K. Elliott, "Absolute potential measurements inside microwave digital ICs using a micromachined photoconductive sampling probe," *IEEE Trans. Microwave Theory Tech.*, vol. 46, pp. 2330-2337 (Dec. 1998).
4. G. David, K. Yang, M. Crites, J.-S. Rieh, P. Bhattacharya, L.P.B. Katehi, and J.F. Whitaker, "Photoconductive probing and computer simulation of microwave potentials inside a SiGe MMIC," in *IEEE Topical Meeting on Silicon Monolithic Integrated Circuits in RF Systems*, S. Kayali, Ed. (IEEE, Piscataway, NJ, Sept. 1998), pp. 187-191.
5. G. David, J.F. Whitaker, T.R. Weatherford, K. Jobe, S. Meyer, M. Bustamante, W. Goyette, S. Thomas III, and K. Elliott, "DC-to-mm-wave absolute potential measurements inside digital microwave ICs using a micromachined photoconductive sampling probe," *IEEE MTT-S International Microwave Symposium Digest 1998*, New York: IEEE, pp. 1333-1336.
6. T. Sosnowski, "High repetition rate femtosecond amplifiers and applications to semiconductor dynamics," PhD. Thesis, 1998.
7. T.S. Sosnowski, T.B. Norris, H.H. Wang, P. Grenier, J.F. Whitaker, and C.Y. Sung, "High-carrier-density electron dynamics in low-temperature-grown GaAs," *Appl. Phys. Lett.*, vol. 70, pp. 3245-3247 (1997).
8. P. Grenier and J.F. Whitaker, "Sub-band gap carrier dynamics in low-temperature-grown GaAs," *Appl. Phys. Lett.*, vol. 70, pp. 1998-2000 (1997).
9. R.K. Lai, J.-R. Hwang, J. Nees, T.B. Norris, and J.F. Whitaker, "Ultrahigh-sensitivity, ultrafast-response photoconductive probe," in *Ultrafast Electronics and Optoelectronics*, Technical Digest (Optical Society of America, Washington, DC, 1997) pp. 175-177.
10. T.S. Sosnowski, T.B. Norris, H.H. Wang, P. Grenier, J.F. Whitaker, and C.Y. Sung, "High-carrier-density pump-probe measurements of low-temperature grown GaAs," in *Ultrafast Electronics and Optoelectronics*, Technical Digest (Optical Society of America, Washington, DC, 1997) pp. 198-200.
11. H.-H. Wang, P. Grenier, J.F. Whitaker, H. Fujioka, J. Jasinski, and Z. Liliental-Weber, "Ultrafast response of As-implanted GaAs photoconductors," *IEEE J. Selected Topics in Quantum Electron.*, vol. 2, pp. 630-635 (1996).
12. W. Walukiewicz, Z. Liliental-Weber, J. Jasinski, M. Almonte, A. Prasad, E.E. Haller, E.R. Weber, P. Grenier, and J.F. Whitaker, "High-resistivity and ultrafast carrier lifetime in argon implanted GaAs," *Appl. Phys. Lett.* vol. 69, pp. 2569-2571 (1996).
13. J.-R. Hwang, R.K. Lai, J. Nees, T.B. Norris, and J.F. Whitaker, "A field-sensitive photoconductive probe for sampling through passivation layers," *Appl. Phys. Lett.*, vol. 69, pp. 2211-2213 (1996).

14. R.K. Lai, J.-R. Hwang, J. Nees, T.B. Norris, and J.F. Whitaker, "A fiber-mounted, micro-machined photoconductive probe with  $15 \text{ nV/Hz}^{1/2}$  sensitivity," *Appl. Phys. Lett.*, vol. 69, pp. 1843-1845 (1996).
15. J.R. Hwang, H.J. Cheng, J.F. Whitaker, and J.V. Rudd, "Modulation bandwidth and noise limit of photoconductive gates," *Optical and Quantum Electronics*, vol. 28, pp. 961-973 (1996).
16. J.-R. Hwang, H.-J. Cheng, J.F. Whitaker, and J.V. Rudd, "Photoconductive sampling with an integrated source follower/amplifier," *Appl. Phys. Lett.*, vol. 68, pp. 1464-1466 (1996).
17. H.-H. Wang, "Nonstoichiometric GaAs-based semiconductors," PhD. Thesis, 1996.
18. J.F. Whitaker, H.H. Wang, C.Y. Sung, T. Sosnowski, T.B. Norris, H. Fujioka, and Z. Liliental-Weber, "Ultrafast carrier response of low-temperature-grown and arsenic-implanted GaAs," *Lithuanian J. of Physics*, vol. 35, pp. 594-600 (1995).
19. H.H. Wang, J.F. Whitaker, K. Al-hemyari, and S.L. Williamson, "Surface passivation and the ultrafast optical response of low-temperature-grown GaAs," in *Defect and Impurity Engineered Semiconductors and Devices*, S. Ashok, J. Chevallier, I. Akasaki, N.M. Johnson, and B.L. Sopori, Eds. (Materials Research Society, Pittsburgh, 1995), pp. 1001-1006.
20. Z. Liliental-Weber, W. Swider, H. Kagiichi, A. Claverie, H.H. Wang, and J.F. Whitaker, "Relation between structure and carrier lifetime in As-implanted GaAs," in *Defect and Impurity Engineered Semiconductors and Devices*, S. Ashok, J. Chevallier, I. Akasaki, N.M. Johnson, and B.L. Sopori, Eds. (Materials Research Society, Pittsburgh, 1995), pp. 677-682.
21. J.F. Whitaker, "Opto-switches using low-temperature MBE GaAs," invited book chapter for *Properties of Gallium Arsenide, 3rd Edition*, M. Brozel and G. Stillman, Eds.

## *VII. Conference Presentations*

1. G. David, J.F. Whitaker, T.R. Weatherford, K. Jobe, S. Meyer, M. Bustamante, W. Goyette, S. Thomas, III, and K. Elliott, "DC-to-mm-wave absolute potential measurements inside digital microwave ICs using a micromachined photoconductive sampling probe," presented at the 1998 IEEE International Microwave Symposium, Baltimore, MD, June 1998.
2. G. David, J.F. Whitaker, E.J. Ledbetter, T.R. Weatherford, D. Fouts, W. Goyette, K. Jobe, and K. Elliott, "A picosecond-response photoconductive-sampling probe for digital circuit testing," presented at the 1997 Annual Meeting of the IEEE Lasers and Electro-Optics Society, Nov. 1997.
3. E. Ledbetter, T. Weatherford, G. David, J. Hayden, R. Lai, and J. Whitaker, "*In situ* picosecond resolution measurements of SEU transients in GaAs logic," presented at the 1997 IEEE Nuclear and Space Radiation Effects Conference, July 1997.
4. T.S. Sosnowski, T.B. Norris, P. Grenier, and J.F. Whitaker, "Defect-enhanced Auger recombination and high-carrier-density phenomena in low-temperature grown GaAs," paper JWA7 presented at the 1997 Conference on Lasers and Electro-Optics.
5. R.K. Lai, J.-R. Hwang, J. Nees, T.B. Norris, and J.F. Whitaker, "Ultra-high-sensitivity, ultrafast-response photoconductive probe," presented at the 1997 OSA topical conference on Ultrafast Electronics and Optoelectronics.
6. T.S. Sosnowski, T.B. Norris, H.H. Wang, P. Grenier, J.F. Whitaker, and C.Y. Sung, "High-carrier-density pump-probe measurements of low-temperature grown GaAs," paper UWB5 presented at the 1997 OSA topical conference on Ultrafast Electronics and Optoelectronics.
7. S.L. Williamson, K. Al-hemyari, H.-J. Cheng, J.-R. Hwang, J.A. Nees, and J.F. Whitaker, "An ultrafast photoconductive sampling gate integrated with a JFET amplifier," presented as an invited paper at the 1996 annual meeting of the Lasers and Electro-Optics Society, Nov. 1996.
8. J.F. Whitaker, H.H. Wang, C.Y. Sung, T. Sosnowski, T.B. Norris, H. Fujioka, and Z. Liliental-Weber, "Ultrafast carrier response of low-temperature-grown and other non-stoichiometric semiconductors," presented as an invited talk at the 9th Symposium on Ultrafast Phenomena in Semiconductors, Vilnius, Lithuania, Sept. 5-7, 1995.
9. J.-R. Hwang, H.-J. Cheng, J.F. Whitaker, and J.V. Rudd, "An ultrafast photoconductive sampling gate integrated with a JFET amplifier," presented at the 1995 annual meeting of the Lasers and Electro-Optics Society, Oct. 1995.
10. T.B. Norris, "Ultrafast High Spatial Resolution," invited tutorial presented at the ILS-XI/OSA Annual Meeting, Portland, 1995.
11. J.F. Whitaker, H.H. Wang, K. Al-Hemyari, and S.L. Williamson, "Ultrafast optical response: Ion-implanted GaAs vs. LT-GaAs," presented at the Workshop on Non-Stoichiometric GaAs and Related Materials, Santa Barbara, CA, March 1996.
12. T.B. Norris, J. F. Whitaker, C.Y. Sung, H.H. Wang, and T. Sosnowski, "Time-Resolved Electron and Hole Trapping and Trap Saturation Dynamics in LT-GaAs," presented at the Workshop on Non-Stoichiometric GaAs and Related Materials, Santa Barbara, CA, March 1996.



13. K. Al-hemyari, H.-J. Cheng, S.L. Williamson, J.-R. Hwang, and J.F. Whitaker, "Ultrafast Sampling with an Amplified, Polyimide-Based Photoconductive Probe," presented at the 1996 OSA Topical Meeting on Ultrafast Phenomena, San Diego, CA, May 1996.
14. C.Y. Sung, H.H. Wang, T.B. Norris, and J.F. Whitaker, "Ultrafast electron and hole trapping times and defect band saturation dynamics in low-temperature grown GaAs," presented at the 1996 Conference on Lasers and Electro-Optics, Anaheim, CA, June 1996.
15. J.-R. Hwang, R.K. Lai, J. Nees, T. Norris, and J.F. Whitaker, "Photoconductive sampling through insulating layers with microvolt sensitivity," presented as a post-deadline paper at the 1996 Conference on Lasers and Electro-Optics, Anaheim, CA, June 1996.
16. F. Garet, L. Duvillaret, G. Angenieux, J.L. Coutaz, and J.F. Whitaker, "THz characterization of substrate materials for electronics," presented at the 1996 Progress in Electromagnetics Research Symposium (PIERS), Innsbruck, Austria, July 1996.
17. J.F. Roux, F. Garet, J.L. Coutaz, J.F. Whitaker, "Non-linear behavior of LT-GaAs photoconducting switches used as Hertzian dipole source for THz spectroscopy," presented at the 1996 Progress in Electromagnetics Research Symposium (PIERS), Innsbruck, Austria, July 1996.

#### *VIII. Inventions, etc.*

There were no patents filed as a result of the research conducted under this support. The discovery of the extreme increase in sensitivity when incorporating the source follower with the photoconductive probe is summarized in Sect. III.B.